Materials Plus
https://ojs.wiserpub.com/index.php/MP/

UNIVERSAL WISER PUBLISHER

Research Article

Kinetics and Products of the Reaction of Graphene Nanoplatelets with Noble Metal Ions to Nanocomposites with Single Atoms and Clusters

Daniel Konradt[1], Detlef Schroden[2], Markus Heidelmann[3], Ulrich Hagemann[3], Hans-Peter Rohns[2], Christoph Wagner[2], Norbert Konradt[2]*

[1] Ruhr-Universität Bochum, Ruhr University Bochum, Faculty of Mechanical Engineering and Faculty of Chemistry and Biochemistry, Universitätsstraße 150, 44801 Bochum, Germany
[2] Stadtwerke Düsseldorf AG, Wiedfeld 50, 40589 Düsseldorf, Germany
[3] ICAN, NETZ Building, Carl-Benz-Straße 199, 47057 Duisburg, Germany
E-mail: norbkonradt@gmx.de

Received: 30 April 2024; **Revised:** 25 May 2024; **Accepted:** 19 June 2024

Abstract: Metal-supported graphene nanocomposites with single atoms or small clusters are of interest for various catalytic processes, including applications in batteries, fuel cells, water electrolysis, and chemical synthesis. Typically, graphene oxide is reduced in the presence of metal salts to produce metal-graphene nanocomposites. However, graphene itself has reductive properties and can react with metal ions in higher oxidation states in a suitable solvent. While direct reactions (dip and coat or wet coating) with metal salts have been described several times, less is known about the kinetics. This study investigates the reaction of suspended graphene nanoplatelets (GNP) in aerated water with the chlorocomplexes of gold (III), iridium (IV), platinum (IV), and palladium (II) to form nanocomposites covered with single atoms and small clusters. The maximum metal loading ranges from 3.3 mass% for palladium to 44 mass% for gold, increasing with redox potential. At high redox potentials, such as those of Ir (IV) and Au (III), the reactions follow pseudo-first order kinetics. In contrast, at lower potentials, such as those of Pt (IV) and Pd (II), the reaction adhere to pseudo-second order. This data enable kinetically controlled metal coating of the GNP. In contrast to the use of a reducing agent, gold, platinum, and palladium are present on the GNP in different oxidation states, which can be specifically modified, as shown for platinum-coated GNP. Iridium (IV) has been deposited as anhydrous and hydrated iridium (IV) oxide. The nanocomposites have great potential as single-atom catalysts. The described process can be transferred to other transition metals and is sustainable because the reaction media can be recycled.

Keywords: graphene nanoplatelets, wet impregnation, noble metal nanocomposites, heterogeneous reactions kinetics, single-atom catalysts, clusters

1. Introduction

The term “single-atom catalysts” (SACs) has been used for more than 15 years, but the first studies were performed as early as 1988. It is currently a very intense area of research and there are many expectations for the further development of catalysis [1]. Since the 1920s, it has been assumed that free adsorption sites on surfaces are crucial for catalysis. The homogeneous polymerization of alkenes was discovered in 1953 with the Ziegler-Natta process, and in the 1960s the

DOI: https://doi.org/10.37256/3220244863

mechanism was elucidated with the identification of coordinatively unsaturated centers, in parallel with the development of other homogeneous catalyzed reactions such as the Wilkinson hydrogenation of alkenes. Results with nanomaterials showed that an improvement in activity was often accompanied by a reduction in active area [1], and research with clusters led to the realization that in many cases a single atom can suffice as a catalytic center [2]. Indeed, there is a strong expectation that SACs can improve future sustainable resource management requirements. Of central interest are the photochemical or electrolytic carbon dioxide reduction reaction (CO_2RR) to C_1 basic chemicals such as CO or methanol, the electrolytic or photochemical oxygen evolution reaction (OER), the hydrogen evolution reaction (HER) [3], and the improvement of the electrochemical oxygen reduction reaction (ORR) for fuel cell applications [4]. In addition to single atoms on support materials, small clusters of less than 13 atoms are also of interest. A cluster is defined by IUPAC as "a number of metal centers grouped closely together, which may have direct metal bonding interactions or interactions through a bridging ligand, but are not necessarily held together by these interactions" [5]. In clusters containing only a small number of metal atoms, only a finite number of quantum states are allowed for their electrons, so they do not form a conduction band like in bulk metals. In this sense, small clusters of metal atoms are more similar to conventional molecules than to solid metals [6]. As catalysts, clusters and single atoms on a support material show the highest activity and result in maximum atom utilization efficiency, which is particularly important for expensive noble metal catalysts. However, as the metal lattice breaks down into clusters and atoms, the surface energy of the system also increases, making it more likely that adatoms will migrate to form larger clusters. The support material therefore has the important role of fixing and stabilizing the single atoms, allowing the adsorption of the educts and the desorption of the products so that the catalytic process can continue.

Carbon materials have always been an important support, especially for noble metal catalysts. Historically, activated carbon was first used as a support for catalysts. Activated carbon has an amorphous structure with a large internal surface area of up to about 1500 $m^2\ g^{-1}$ for technical materials, and corresponding noble metal catalysts are still used today. Activated carbon is also a well-known adsorbent for metal species, e.g., in water treatment. The main binding mechanisms are physisorption and chemisorption. If the metal ions have a high oxidation potential (ORP), a redox reaction takes place and the reduction product is bound to the carbon [7]. The metal uptake can often be described by pseudo-first order or pseudo-second order kinetics, whereby the carbon is not included in the rate equation due to the large excess [8]. A synthesis library of almost all possible elements of the periodic table on porous nitrogen-containing carbon is available [9]. However, the support material is amorphous, the type of bonding of the adatoms and the coordination environment are not defined.

Two-dimensional graphene is of particular interest as a support material for single-atom catalysts because it has a defined planar structure and there are many theoretical studies on the bonding of the adatoms [3,4,10–13]. Graphene consists of honeycomb fused benzene rings that host delocalized π-electrons both above and below the plane, resulting in a small bandgap semiconductor with a band overlap of 0.16 meV [14,15]. The band gap increases with the number of layers, and with 11 layers the difference from semi-metallic graphite (41 meV) is only 10%, indicating a significant loss of this nanomaterial property [16]. Graphene also has interesting mechanical properties such as a high elastic modulus of ~1 TPa, a high tensile strength of 130 GPa and a breaking strength of 42 Nm^{-1}, which is important for use in demanding reaction conditions [17]. As a carbon material, graphene is a reducing agent, as evidenced by its reactions with oxidative reagents such as oxygen at elevated temperatures [18], hydrogen peroxide [19], or oxometalates [20]. In contrast to pure oxygen, sorption from the ambient air is only partially reversible [21]. Single-layer graphene is not typically found as a bulk material; instead, multiple graphene layers are often stacked to form few or multilayer graphene. When the lateral extent in two dimensions is significantly larger than the thickness, the materials are referred to as nanosheets or nanoplates [22]. The graphene nanoplatelets (GNP) used in this study are patented [23], manufactured by XG Science, and well characterized [20,24,25]. They have a sufficiently large specific surface area for metal sorption of 750 $m^2\ g^{-1}$, while the maximum value of single layer graphene is 4 times higher (~2630 $m^2\ g^{-1}$). These GNP are produced by microwave exfoliation of acid-intercalated graphite and consist of stacks of up to eleven graphene layers with a diameter of <5 μm [20]. While the process ensures that the basal planes remain intact, the edges are substituted with hydroxyl and carboxyl groups during the process, making the material more polar than graphene. XG Science's GNP were dispersible in water, which is not the case for all graphene materials [26]. DLS measurements of GNP in deionized water (DI) showed that the particle size was smaller than 1 μm, which is within the specification (<2 μm). In the presence of salty water (700 $\mu S\ cm^{-1}$), the particle size increases to the average of 15

μm. Under these conditions, the microparticles can be easily separated using a filter or a ceramic filter frit, allowing the concentration to be determined at-line [20].

In the literature, most reactions of noble metal salts with graphene oxide (GO) or regenerated GO (rGO) have been carried out with a high defect content and an increased oxygen content in contrast to GNP [27]. The synthesis often starts with the Hummer reaction, a complex oxidation of graphite powder with potassium permanganate in sulfuric acid, occasionally with the addition of sodium nitrate or subsequent treatment with hydrogen peroxide. The drastic oxidative conditions lead to GO with variable structures and properties, where, in contrast to GNP, part of the aromatic structures of the graphene layers are destroyed by oxidation. Nevertheless, GO shows an adsorption of metal ions, which is mainly based on electrostatic forces [28].

If GO is reacted with reductants as hydrazine or thermally treated at high temperatures, a part of the graphene layer structure was restored, but as with GO synthesis, reaction products can hardly be reproduced. Like GNP, rGO is dispersible in water and has reducing properties, resulting in reactions with metals in higher oxidation states. However, GO and rGO have often been successfully used in the preparation of catalysts [29,30]. In common approaches, chemically synthesized colloidal graphene oxide is physically or chemically linked to in-situ generated metallic nanoparticles by hydrophobic interaction, electrostatic interaction or covalent bonding. Alternatively, noble metal hydroxides can be prepared in colloidal form, which adsorb on the GO and are subsequently reduced to the metallic state [29]. The adsorption isotherms for gold (III), palladium (II), and platinum (IV) on GO were measured and obeyed the Langmuir equation, and the adsorption kinetics followed a pseudo-second order law, indicating that chemical adsorption was the rate-limiting step [31]. Alternatively, noble metal hydroxides can be prepared in colloidal form, adsorbed on GO, and subsequently reduced to the metallic state [29]. Similar to the approach used in this study, a water-based synthesis of a gold/rGO nanocomposite without additional reducing agent has been reported, yielding gold nanoparticles with an average size of 1.8 nm on the support material, which showed excellent electrocatalytic performance for ORR [32]. The study also described the analogous synthesis of a palladium nanocomposite starting from palladium (II), which led to palladium nanoparticles with an average diameter of 1.4 nm on rGO. However, hexachloroplatinate (IV) reacted only partially with GO, while some remained as platinum (II) in solution. Therefore, sodium borohydride was used as a reducing agent. Platinum nanoparticles with an average size of 1.9 nm were then formed on the rGO. However, single atoms or small clusters were not detected in this study.

In contrast, GNP have rarely been used. The synthesis of a hydrogenation catalyst has been described. After wet impregnation of GNP with the precursor palladium (II) acetate for 30 min at room temperature, formaldehyde was used as a reducing agent and sodium hydroxide to enhance particle nucleation. After filtration and drying at 100 °C, a GNP nanocomposite with 1% palladium and metal nanoparticles of size (3.7 ± 1.7) nm was obtained [33]. An electrocatalyst for PEM fuel cells was synthesized by a thermodynamically controlled platinum deposition on GNP using (1,5-cyclooctadiene)dimethyl platinum (II) in supercritical carbon dioxide with different concentrations. The resulting platinum/GNP nanocomposites contained 12.2 to 25.7 wt.% Pt and had a size of 1.5 nm to 1.9 nm [34]. In these case, GNP could be covered by noble metal nanoparticles, but the concentrations were higher and no kinetic data were collected. Relevant to this work is a study on the preparation of defect-free GNP by an ultrasonic process and subsequent reaction with gold (III) acetate in aqueous solution, which resulted in gold nanoparticles on the GNP. The size of the nanoparticles (8.3 to 23 nm) depended on the concentration of gold acetate, which was varied between 1 and 10 mol%. For comparison, a 1 mol% tetrachloroauric acid was tested and smaller nanoparticles with an average size of 1.8 nm were formed, but the material was not further characterized [35].

The role of the metal in single atom catalysis is important because the reaction is supposed to take place at the metallic center. Graphene acts as a support and stabilizes single atoms, which have a strong tendency to form larger clusters with different properties. In addition, there is an electronic interaction with the graphene conduction band. This changes the catalytic properties of the metals in a defined direction. Noble metal SACs are of particular interest due to their high catalytic activity and stability against reduction, oxidation and poisoning. The 5d elements gold, platinum and iridium and the 4d element palladium are of particular interest due to their wide application and stability and are therefore considered in this article.

Gold (Au) is situated in group 11 of the PSE with [Xe] $4f^{14}$ $5d^{10}$ $6s^{1}$ electron configuration and is the element with the highest electron affinity (2.31 eV). Although the bulk metal is less reactive, the compounds have extensive applications

in pharmaceuticals and catalysis[36]. In addition to the metallic form, the +1 and +3 oxidation states are important. Less common are +2 compounds, which are usually diamagnetic and have Au-Au bonds, as in $[Au(CH_2)_2P(C_6H_5)_2]_2Cl_2$. Gold (I) compounds with d_{10} electron configuration prefer a linear geometry, form chains in the solid state, and tend to disproportionate into metallic gold and Au (III) if not stabilized with ligands. Gold (I) chloride is a yellow solid that can be produced from tetrachloroauric acid (III) by thermal decomposition. It has a zigzag chain structure in which gold and chloride ions alternate. Dark purple gold (I) hydroxide precipitates from gold (III) solutions with alkaline hydroxide in the presence of reducing agents[37]. Gold (III) chloride ($AuCl_3$) is the most commonly used gold compound, which is complexed by hydrochloric acid to form tetrachloroauric acid. The neutral or basic solution of the planar $[AuCl_4]$ with d_8 electron configuration is susceptible to hydrolysis. When the tetrachloroaurate solution is alkalized, a brown precipitate of gold (III) hydroxide is formed, which cannot be isolated but is converted to brown gold (III) oxide on drying. Above 160 °C it decomposes to gold (I) oxide and elemental gold[37], with light accelerating the reaction[36]. Gold clusters are already known from complex chemistry, mostly stabilized with phosphine ligands, as in $[Au_6C(P(C_6H_5)_3)_6]^{2+}$[38]. Gold catalysis has been demonstrated for many reactions, especially oxidation, reduction, and C-C coupling[39,40]. The structural relationships between single atom catalysts and catalytic activity have been studied mainly on supported gold[3]. In 1988, the first single-atom catalysis using gold on carbon support in the gas phase hydrochlorination of acetylene was reported[41]. At the same time, the high activity of gold nanoparticles on transition metal oxides in the oxidation of carbon monoxide was demonstrated[42].

Platinum (Pt) is a group 10 element within the PSE with a [Xe] $4f_{14}$ $5d^9$ $6s^1$ electron configuration and has the second highest electron affinity at 2.13 eV. Unless the metal is finely dispersed, it has low reactivity. Important oxidation states are +2 and +4, less common are +1 and +3, which are often stabilized by metal bonds. Platinum (II) compounds are often four-coordinate and tend to adopt square-planar 16-electron geometries, but five-coordinate species are also known[43]. Black hydrous platinum (II) oxide precipitates from tetrachloroplatinate (II) solutions with alkali metal hydroxide, cannot be dehydrated to PtO, but instead forms a platinum (III) oxide hydrate that readily oxidizes to platinum dioxide in air[37]. The potassium salt of chloroplatinic acid (K_2PtCl_6) is an important commercial chemical in the +4 oxidation state, where the Pt is octahedrally coordinated by six chloride ions. In industrial applications, platinum is used for electrocatalysis in PEM technology as platinum black in electrolysis, and platinum dioxide has applications as a catalyst for hydrogenation and ammonia oxidation[43]. Platinum nanoparticles on rGO are a stable catalyst that can improve the performance of fuel cells[44]. Platinum is the most versatile element in single atom catalysis (SAC) with numerous applications in oxidation and reduction reactions as well as electro- and photocatalysis[3].

Iridium (Ir) is a member of group 9 of the PSE with electron configuration [Xe] $4f^{14}5d^76s^2$. In addition to the metallic form, important oxidation states are +1, +3, and +4. Iridium (I) is often found in carbonyl metalate complexes or carbonyl compounds with ligands such as triphenylphosphine. Iridium (III) complexes are primarily octahedral, but five-coordinate stereochemistry is also known. In alkaline Ir (III) solutions, green iridium (III) hydroxide precipitates, which is oxidized in air to blue iridium dioxide[37]. Apart from the rutile type IrO_2, only an amorphous oxide IrO_x is known, which has a defect structure with 80% Ir (IV) and 20% Ir (III) cations and about 40% O (I) and 60% O (II) anions[45]. The most common oxidation state is +4 with an octahedral geometry. The ammonium salt hexachloroiridate (IV), $(NH_4)_2IrCl_6$, is an important compound for both preparative and industrial applications[37]. The tetrachloroiridate (IV) ion has an intense dark brown color and is easily reduced to the light brown iridate (III), which is an important catalyst and finds application in hydrogenation, hydrogen transfer, C-H bond functionalization, allylic substitution, carbonylation, and 1,3-dipolar cycloaddition[46]. Electrodes coated with iridium nanoparticles can be used for electrocatalysis[44]. Iridium SACs are used for hydrogenation, oxidation and reduction, electrocatalysis and photocatalysis[3].

Palladium (Pd), a member of group 10 in the PSE with a [Kr] $4d^{10}5s^0$ electron configuration, occurs predominantly in oxidation states 0 and +2, more rarely in the oxidation states +1 and +4. Pd (0) complexes are known with various ligands and typically have the stoichiometries $[PdL_4]$, $[PdL_3]$ and $[PdL_2]$[37,43]. Metallic palladium can absorb significant amounts of hydrogen and form stable carbon bonds. Pd (II) compounds are typically four-coordinate, square-planar, but five-coordinate compounds are also common[47]. Diammonium palladate (II), $(NH_4)_2PdCl_4$, is a commonly used chemical and is also used as a reactant here. Insoluble palladium (II) oxide hydrate and palladium dioxide hydrate are obtained by precipitation from the corresponding chlorocomplexes with alkali metal hydroxides, with PdO being the more potent

oxidant[37]. The preparation, characterization and catalytic activity of Pd nanoparticles have been reviewed[48]. Recently, the construction of a square PdO network with lateral dimensions up to hundreds of nanometers on rGO has been reported[49]. Palladium nanoparticles find applications in fuel cells, hydrogen storage, and sensors for gases such as hydrogen[50,51]. In the case of trimerization of acetylene, it has been demonstrated that only one palladium atom is sufficient to catalyze the process[52]. Pd-SACs can be used as catalysts for cross-coupling reaction, C-H activation, C-O oxidation, electro- and photocatalysis, and transfer hydrogenation[3]. A synthesis of Pd single atoms on rGO has been published[53], while the synthesis of Pd on GNP has not been reported yet[54].

Despite numerous catalyzed reactions with SACs, hardly any of them have successfully found their way into technical implementation[55]. In addition to the fact that established reactions with conventional catalysts are constantly being optimized, which represents a high hurdle for new catalyst technologies, other reasons include problems with the stability of the metal-support interactions, the control over the ligand sphere, the influence of the reaction medium and the dynamic behavior during the process[56]. Furthermore, the existing oxidation states are rarely taken into account and an averaged valence is used instead[3], although it is certain that each oxidation state of an element has a different activity in a given process. The fact that the individual oxidation states have an important influence on the catalyzed reaction has only recently been taken into account[57,58]. Furthermore, the possibility of separately modifying specific oxidation states through a selective reaction has rarely been considered. An example is the catalysis with single Pt atoms on defective ceria with controlled oxidation state of Pt-SACs from highly oxidized (Pt (0): 16.6 atom %) to highly metallic states (Pt (0): 83.8 atom %). The Pt-SACs were used for the oxidation of carbon monoxide, methane or nitric oxide, with the metallic Pt-SACs showing higher activities[59]. Similar experiments with Pd/PdO catalysts from 2 to 5 nm on GO/rGO support with different compositions for the electrooxidation of methanol revealed an optimal size of 2.2 nm and that mixed-valent oxygenated platinum offers better CO tolerance and long-term catalyst stability[44].

While earlier studies aimed to produce metallic nanoparticles with high coverage in a single oxidation state, usually zero valence, the current focus is on fixing single atoms and small clusters in a well-defined environment[3]. In addition, the different properties of the oxidation states are receiving increasing attention. In this work, the results of the direct reaction of graphene nanoplatelets with noble metal salts in higher oxidation states and correspondingly high redox potentials are presented. We chose a wet synthesis in aerated water at low noble metal concentrations and high mixing for gold (III), platinum (IV), iridium (IV), and palladium (II) using graphene nanoplatelets (GNP) from XG Science without additional reducing agents. The heterogenous reaction is performed at high dilution, high stirring rate and with kinetic control, which allows a predictable coverage of the graphene substrate. To control the process, the sorption was monitored using at-line UV-Vis spectrometry and the kinetics of the sorption was determined. Since GNP adsorb water and oxygen when stored at ambient conditions, a GNP sample was thermally regenerated[21] and its reactivity towards palladium (II) was tested. Thermal regeneration can be beneficial for some substrates, e.g., chromium (VI), but reduce the rate constant and coverage for others, e.g., vanadate (V)[20]. The resulting nanocomposites were analyzed by XPS for elemental composition and oxidation states, and by STEM to evaluate the size and distribution of noble metals.

2. Materials and methods

2.1 *Reagents*

All reagents used were analytical grade unless otherwise stated. Gold (III) chloride, 30% wt.% in dilute HCl (auric acid, $HAuCl_4$), 99.99% trace metals basis (Cat. No. 484385) and sodium 2-mercaptoethanesulfonate, MESNA (Cat. No. M1511) were purchased from Sigma-Aldrich, Taufkirchen, Germany. Ammonium tetrachloropalladate (II) (10824) and ammonium hexachloroiridate (IV) (10712) were purchased from Alfa Aesar, MA, USA. Potassium hexachloroplatinate (IV) (119238), sodium hydroxide 0.1 M (1.09141), and hydrochloric acid 0.1 M (1.01145) were purchased from Merck KGaA, Darmstadt, Germany. Deionized water (DI) with a conductivity of >17.6 MΩ cm^{-1} was prepared using a 2-stage Berkefeld system from Veolia Water Technologies Deutschland GmbH, Celle, Germany. The air-saturated, salt-containing water (AW) had an electric conductivity of ~700 µS cm^{-1} and a pH of ~7.0. The ionic composition was calcium (2.0 mM),

magnesium (0.77 mM), sodium (1.75 mM), chloride (2.82 mM), sulfate (0.57 mM), and bicarbonate (3.28 mM). The total organic carbon content was <0.3 mg L^{-1}.

Graphene nanoplatelets (xGnP®, grade C, thickness <4 nm, lateral size <2 μm) with a surface area of 750 m^2 g^{-1} were purchased from Sigma-Aldrich, Darmstadt, Germany, manufactured by XG Sciences, Lansing, MI, USA, and used as they were received. Due to the propensity of GNP to absorb water, gases and airborne contaminants from the environment, the material was stored in a sealed container. Elemental analysis revealed the the main elements in Table 1 [20].

Table 1. Elemental analysis of graphene nanoplatelets (GNP) [1]

Sample	C (%)	H (%)	N (%)	S (%)	K (%)	Mg (%)	Ca (%)	O_{calc} (%)	Drying Loss (%)
GNP	89.21	0.57	0.89	0.07	0.04	0.03	0.06	9.13	7.7
GNP reg[2]	89.40	0.50	1.00	0.10	0	0.03	0.10	8.87	2.2

[1] Data taken from [20]; [2] GNP regenerated at 1050 °C (Section 2.2)

The GNP were characterized as stacks of 4 to 11 graphene layers for the XG graphene nanoplatelets with partially disordered structures on the upper graphene layer. The Raman spectra showed an intensity-to-height ratio of I_D/I_G of 0.98 for GNP and of 0.92 for thermally regenerated GNP (GNP reg), indicating multilayer graphene with some disorder [20].

2.2 *Methods*

Solid samples were analyzed by XPS using an Ulvac-Phi VersaProbe II equipped with a monochromatic Al Kα light source with a photon energy of 1486.6 eV and a beam diameter of 100 μm. The angle between the sample and the analyzer was 45°. STEM and STEM-EDS were measured with a JEOL JEM-2200 FS FE-TEM, 200 KV. Electrical conductivity (EC), pH value, oxidation reduction potential (ORP), dissolved oxygen, and temperature were measured and recorded with a Multi 3430 IDS connected to TetraCon® 925, SenTix® 980P, SensoLyt®, SenTix® or ORP 900P sensors from WTW, Weinheim, Germany. Microscopy was performed with a digital microscope AF4115ZT, magnification 20–220× from Dino-Lite Europe, Manuscriptstraat 12–14, Almere, The Netherlands. UV-Vis measurements were performed using a Lambda 35 spectrophotometer with WIN-LAB software, version 6.0.3, PerkinElmer Life and Analytical Sciences, Shelton, CT, USA, equipped with a 50 mm flow cell (high performance quartz glass 200–2500 nm, Cat. No. 176,700, volume 2.25 mL, Hellma GmbH & Co. KG, Müllheim, Germany).

For one experiment, 250 mL of water (AW) or 10 mM HCl was filled into a three-necked flask equipped with temperature, pH, and EC sensors. A ceramic or metallic filter frit (5 μm) was inserted and the filtrate was continuously pumped with a cassette pump (model 205U Watson Marlow, Rommerskirchen, Germany) through a Tygon tube (SC0017T, Ismatec, Wertheim, Germany) at a flow rate of 9 mL min^{-1} through the cuvette placed in the photometer and then back into the flask. The UV-Vis spectrometer was set to the corresponding wavelength in Table 2, slit width 1 nm, running time 10–60 min with appropriate time period, the background was recorded and set to zero. For mass determinations in the range from 10–1000 mg, an XS204 analytical balance (repeatability 0.1 mg) from Sartorius, Göttingen, Germany, was used. Stock solutions of potassium tetrachloroplatinate (IV) (5 mM), ammonium tetrachloroiridate (IV) (10 mM), and auric acid (10 mM) were prepared by dissolving the respective salt or solution in DI and stored in the dark. The respective stock solution was added to the water to obtain a noble metal solution of a defined concentration. In the case of ammonium tetrachloropalladate (II), the salt was weighed and added directly to the solvent with stirring (800 rpm) at room temperature. After stabilization of the UV-Vis absorption (3–5 min), a certain mass of GNP was added and the time-dependent decrease of the metal ion UV-Vis absorption was measured. In water with low salinity, nanoparticles aggregate into microparticles that are easily retained by a filter. The decrease in metal ion concentration was calculated as c_t/c_0, where c_0 is the initial concentration before the addition of GNP. In some cases, further additions of metal salts were required to achieve maximum coverage of the remaining metal concentration in the solution. At the end of the reaction, the precipitate was filtered (0.45 μm), washed three times with deionized water, and air dried. The solids were analyzed by scanning transmission electron microscopy (STEM), energy dispersive spectroscopy (EDS) and X-ray photoelectron

spectroscopy (XPS). Fixation of platinum on GNP for STEM analysis was achieved by treating the reacted GNP in 50 mL of deionized water with 20 mg MESNA in an ultrasonic bath for 30 min[61]. The suspension was filtered (0.45 μm) and the solid was washed with ethanol/water and air dried. The solid was analyzed using XPS and STEM.

Table 2. LMCT UV-Vis absorption bands used for noble metal ion quantification

Noble Metal Compound	Solvent	Wavelength (nm)	Absorption Coefficient (M^{-1} cm^{-1})	Literature
Tetrachloroauric acid (III)	deionate	290	3885	[62]
Potassium hexachloroplatinate (IV)	deionate	260	19,956	[63]
Diammonium hexachloroiridate (IV)	deionate	489	1754	[64]
Diammonium tetrachloropalladate (II)	10 mM HCl	425	199.5	[65]

Tetrachloroaurate (III) is susceptible to hydrolysis upon dilution and the absorption maximum for the stock solution at 312 nm in 0.1 mM solution showed a blue shift to the observed 290 nm, corresponding to partial hydrolysis upon pH increase[62]. Further dilution to 0.04 mM did not result in any further change. Since the stock solutions of palladium (II) chloride were turbid after preparation, 10 mM hydrochloric acid solutions were used. Nevertheless, a shift to higher wavelengths from 418 to 425 nm was observed in the spectrum of Pd (II), corresponding to the species $[PdCl_n(H_2O)_{4-n}]^{2-n}$ (n = 2–3)[66].

The oxidation-reduction potentials (ORP) of oxometalates were measured in AW or 10 mM HCl with air contact in a three-necked flask equipped with the ORP electrode, thermometer, and pH sensor. Before use, the ORP electrode was checked with ORP Buffer 220 mV, pH 7 (UH = 427 mV), Cat. No. 51.350.060 (Mettler-Toledo GmbH, Greifensee, Switzerland) and redox buffer 475 mV (UH = 682 mV), Cat. No. 238.322 (Hamilton Bonaduz AG, Bonaduz, Switzerland). ORP was equilibrated in the respective water for up to 20 min with stirring (200 rpm). The measurement was then started at one measurement per minute for 15 min to record the matrix background. The metal ion stock solution was added to obtain the appropriate concentration and the change in redox potential was measured for 15 min until the difference between consecutive measurements was less than 2 mV. The average of 4 consecutive measurements was calculated and the difference was attributed to the influence of the metal ion.

For thermal regeneration of GNP, a tube furnace (model R50/250/12, Nabertherm GmbH, Lilienthal, Germany) equipped with a quartz glass tube with adjustable permanent nitrogen flow was used. The GNP (600 mg) was weighed in a quartz crucible and placed in the unheated part of the furnace and, after temperature equilibration, transferred to the hot zone (1050 °C)[21]. After 30 s, the crucible was removed and allowed to cool in the unheated zone. The GNP reg were transferred to a nitrogen flushed Schlenk flask and stored until use.

3. Results

3.1 *Sorption of gold (III), platinum (IV), iridium (IV), and palladium (II) on GNP*

Chloride complexes of gold (III), platinum (IV), and palladium (II) reacted with GNP in aerated water (AW) at room temperature without the formation of significant by-products. In contrast, iridium (IV) partially formed a dissolved by-product. The reaction progress can be monitored by UV-Vis spectrometry at the specific wavelengths of ligand-to-metal charge transfer (LMCT) (Table 2). The characteristics of the kinetic runs are summarized in Table 3. Concentration-time profiles for the metal ions with empirical curve fitting and the best kinetic evaluation are given in Sections 3.2.1–3.2.4.

Table 3. Basic data for kinetic measurements of noble metal ions with GNP

Process	Runtime (min)[5]	T_m (°C)	pH Start	EC (µS cm^{-1})	$\tau_{1/2}$ Exp (min)	Metal Capacity (Mass%)
0.04 mM $AuCl_3$ in 250 mL AW, 100 mg GNP[1]	4 (30)	21.6 ± 0.1	6.98	707	0.50	38
0.04 mM K_2PtCl_6 in 250 mL AW, 100 mg GNP[2]	15 (60)	24.8 ± 0.2	7.51	696	1.0	8.7
0.2 mM $(NH_4)_2IrCl_6$ in 250 mL AW, 100 mg GNP[3]	11 (30)	21.0 ± 0.6	7.34	669	0.32	33
0.4 mM $(NH_4)_2PdCl_4$ in 250 mL 10 mM HCl, 500 mg GNP[4]	20 (30)	24.0 ± 0.1	2.05	4000	0.75	2.0
0.4 mM $(NH_4)_2PdCl_4$ in 250 mL 10 mM HCl, 500 mg GNP reg[4]	20 (30)	24.0 ± 0.1	2.08	4120	2.5	1.2

Total dosages: [1] 0.31 mmol Au (III), [2] 0.03 mmol Pt (IV), [3] 0.26 mmol Ir (IV), [4] 0.10 mmol Pd (II); [5] total running time in brackets

The sorption of noble metal ions occurred with half times ($\tau_{1/2}$) within minutes, decreasing in the order Ir>Au>Pt (IV)>Pd (II). After metal fixation on GNP, UV-Vis data showed capacities ranging from ~1.2 mass% for palladium to ~38 mass% for gold, increasing in the order Pd (II)<Pt (IV)<Ir (IV)<Au (III). GNP regenerated at 1050 °C was tested for sorption of palladium (II) with the lowest reactivity towards GNP, but the experimental half-life was higher and the coverage was lower than non-regenerated GNP.

3.2 *Evaluation of kinetic schemes*

For the interpretation of experimental data from sorption processes, two main models are commonly discussed, namely pseudo-first order sorption (PFO) and pseudo-second order sorption (PSO)[67]. In addition, the metal ions can react directly with the GNP with pseudo-first or pseudo-second order kinetics (Table 4).

Table 4. Kinetic schemes used for data analysis

Kinetic Type	Linearized Model Form	Linear Plot	Parameter[1]	Equation
Pseudo-first order adsorption	$\ln\left[\frac{q_e}{q_e-q(t)}\right] = k_t$	$\ln\left[\frac{q_e}{q_e-q(t)}\right]$ vst	q_e: determined experimentally, k_1 = m	(1)
Pseudo-second order adsorption	$\frac{1}{q(t)} = \frac{1}{k_2 {q_e}^2\left(\frac{1}{t}\right)}$	$\frac{1}{q(t)}$ $vs\left(\frac{1}{t}\right)$	$q_e = \mathrm{b}^{-1}$, $k_2 = b^2/\mathrm{m}$	(2)
Pseudo-first order reaction	$\ln c = -k_1 t$	$\ln c$ vs t	$k_1 = -\mathrm{m}$	(3)
Pseudo-second order reaction	$\frac{1}{c} = k_2 t$	$\frac{1}{c}$ vs t	$k_2 = \mathrm{m}$	(4)

[1] m: slope; b: intercept; [2] [68]

For regression analysis, the UV-Vis kinetic data were reduced to a maximum of 30 data pairs and fitted to different models[69]. The linearized formulas shown in Table 4 were used for evaluation. The linear parameter fitting was based on the routine of Bevington and Robinson[70]. The adjusted coefficient of variation (R^2 adj), which takes into account the number of measurements, was calculated as an indicator of model performance, with a minimum value of 0.98. In addition, a graphical analysis of the residuals was performed[69], looking for a uniform distribution of the residuals in terms of size and sign (non-randomness and normality test). Under these conditions, only one model was appropriate for each noble metal salt. The regression curves are plotted for each metal. The resulting regression parameters are summarized in Table 5.

Table 5. Best fit kinetic data of reaction of noble metal ions with GNP [1]

Process	Kinetic Type	Data for Regression	Evaluation Time (min)	k_1 (min^{-1})	R^2 adj
0.04 mM $HAuCl_4$ in 250 mL AW, 100 mg GNP	1st	11	1.67–3.33	2.19 ± 0.05	0.9901
0.2 mM $(NH_4)_2IrCl_6$ in 250 mL AW, 100 mg GNP, 1. dosage	1st	25	8.20–9.90	3.1 ± 0.1	0.9834
0.2 mM $(NH_4)_2IrCl_6$ in 250 mL AW, 100 mg GNP, 2. dosage	1st	30	16.6–19.5	0.287 ± 0.001	0.9996
				k_2 (mM^{-1} min^{-1})	
0.04 mM K_2PtCl_6 in 250 mL DI, 100 mg GNP, 1. dosage	2nd	30	2.50–7.33	27.0 ± 0.1	0.9978
0.04 mM K_2PtCl_6 in 250 mL DI, 100 mg GNP, 2. dosage	2nd	15	20.5–27.5	5.14 ± 0.05	0.9946
0.04 mM K_2PtCl_6 in 250 mL DI, 100 mg GNP, 3. dosage	2nd	23	36.0–58.0	1.84 ± 0.01	0.9924
0.4 mM $(NH_4)_2PdCl_4$ in 10 mM HCl, 500 mg GNP	2nd	24	3.82–4.20	8.1 ± 0.1	0.9822
0.4 mM $(NH_4)_2PdCl_4$ in 10 mM HCl, 500 mg GNP reg	2nd	16	3.72–3.97	2.97 ± 0.05	0.9860

[1] Errors of rate constants were multiplied by the statistical factor of 3

After an initial phase in which the GNP were dispersed, gold (III) and iridium (IV) can be fitted to pseudo-first order reaction kinetics with high R^2 adj values, while platinum (IV) and palladium (II) are best fitted to pseudo-second order reaction kinetics.

3.2.1 *Kinetics of Au (III) with GNP*

The auric acid solution (0.04 mM) reacted rapidly with 100 mg GNP dispersed in AW. The process is best fitted to pseudo-first order kinetics (Equation (3)) from 1.67 to 3.33 min with a rate constant of k_{obs} 2.19 ± 0.05 min^{-1} (Table 5). The time-dependent decrease in Au (III) concentration and the pseudo-first order evaluation are shown in Figure 1.

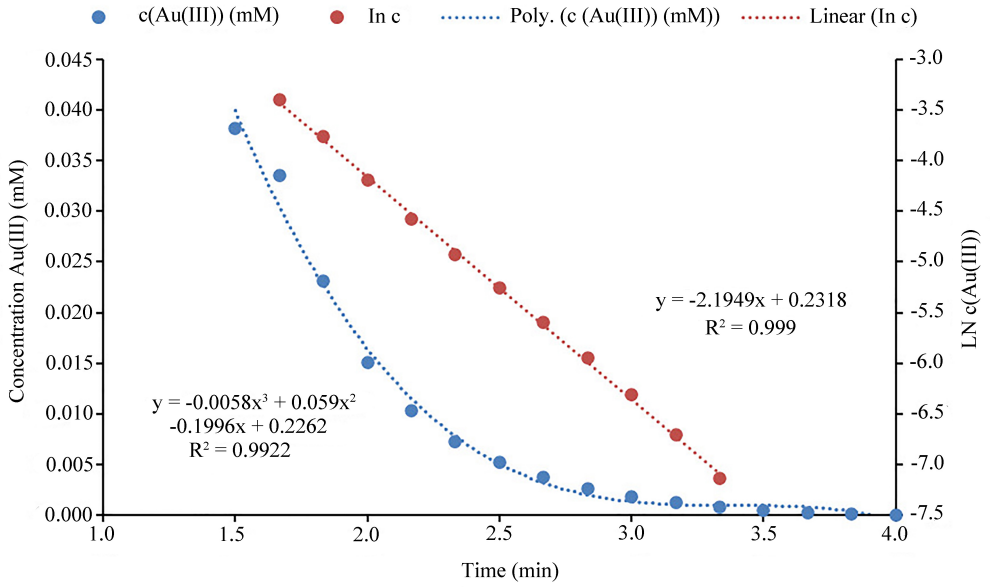

Figure 1. Kinetics of 0.04 mM $AuCl_3$ with 100 mg GNP in AW with an empirical function (blue) and pseudo-first order evaluation (red)

Two further doses of Au (III) were applied after 5 min (0.028 mmol) and 30 min (0.28 mmol). After 24 h, the Au-GNP nanocomposite was isolated and analyzed by STEM and XPS (Section 3.4.1).

3.2.2 *Kinetics of Ir (IV) with GNP*

Graphene nanoplatelets (100 mg) were reacted with 0.2 mM ammonium hexachlororidate (IV) in AW. The reaction can be evaluated from 8.20 to 9.90 min according to pseudo-first order kinetics (Equation (3)) with a rate constant of k_{obs} 3.1 ± 0.1 min^{-1} (Table 5). The time-dependent decrease of Ir (IV) and the pseudo-first order plot are shown in Figure 2A.

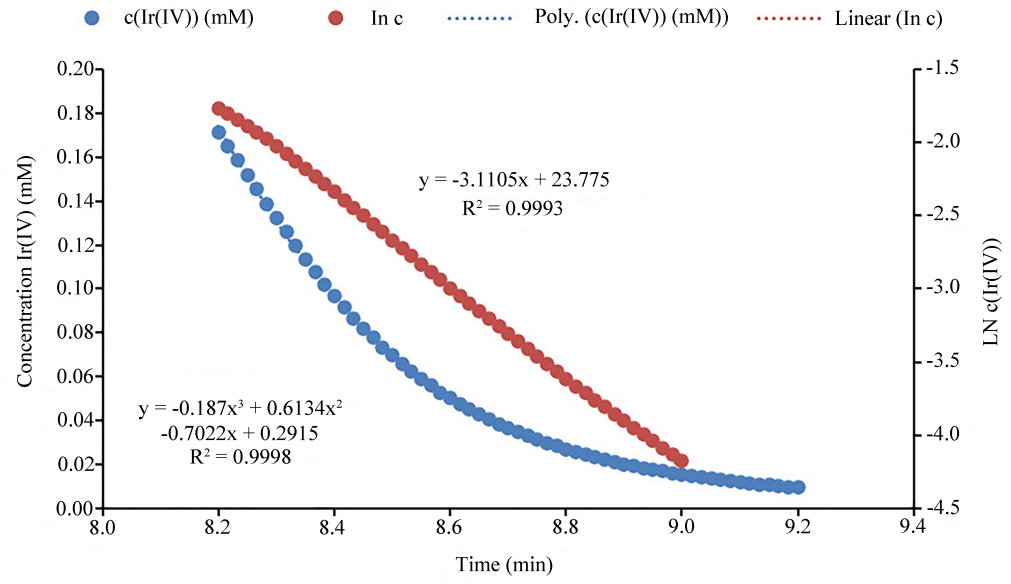

(A)

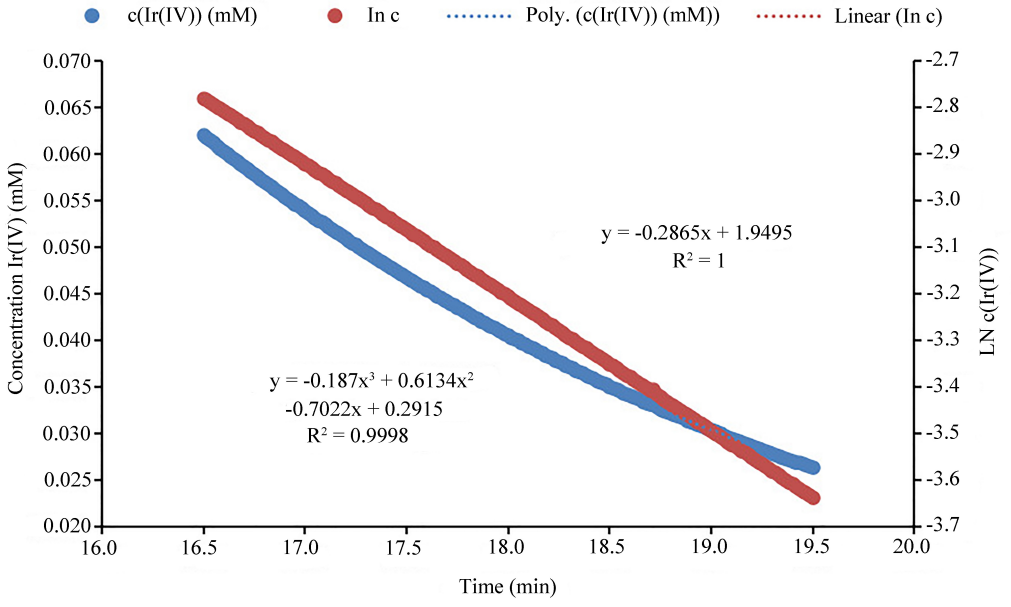

(B)

Figure 2. (**A**) Kinetics of 0.2 mM $(NH_4)_2IrCl_6$ with 100 mg GNP in AW with an empirical function (blue) and the pseudo-first order evaluation (red); (**B**) second dosage of 0.2 mM $(NH_4)_2IrCl_6$

With the second dose of 0.2 mM Ir (IV) the coverage reached almost equilibrium (Figure 2B). The reaction can be best fitted to pseudo-first order kinetics from 16.6 to 19.5 min with a rate constant of k_{obs} 0.287 ± 0.001 min^{-1} (Table 5). The time dependent decrease of Ir (IV) and the pseudo first order evaluation are shown in Figure 2B.

The reaction of $(NH_4)_2IrCl_6$ with GNP in water at neutral pH resulted, in addition to the reaction to Ir-GNP, in a soluble product with a specific UV-Vis spectrum comparable to that of the starting material, but shifted to shorter wavelengths around ~48 nm (Figure 3). After 24 h, the solid product was separated and the Ir-GNP nanocomposite was analyzed by STEM and XPS (Section 3.4.2).

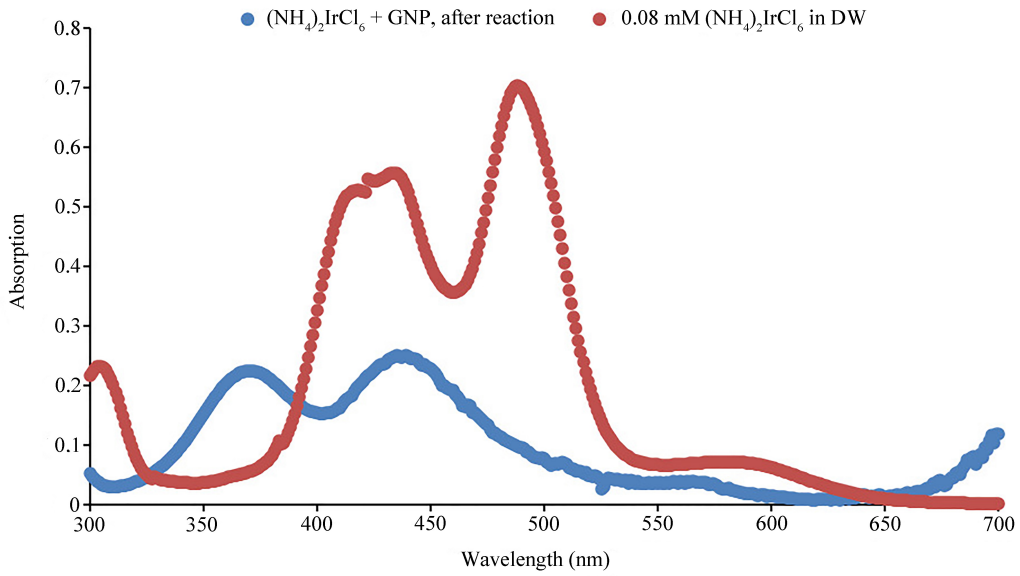

Figure 3. Spectra of 0.08 mM $(NH_4)_2IrCl_6$ (red) before and the after reaction with 100 mg GNP in AW (blue) with maxima at 370 nm and 439 nm

Since the soluble product had a UV-Vis spectrum similar to $[IrCl_6]^{3-}$ produced by electrochemical reduction with maxima at 360 nm and 425 nm[64,71], it can be identified as an iridium (III) hexachloro anion.

3.2.3 *Kinetics of Pt (IV) with GNP*

Graphene nanoplatelets (100 mg) reacted with 0.04 mM potassium hexachloroplatinate (IV) in AW. The reaction can be fitted to pseudo-second order kinetics (Equation (4)) from 2.50 to 7.33 min with a rate constant of kobs 27.0 ± 0.1 M^{-1} min^{-1} (Table 5). The time-dependent decrease of Pt (IV) and the pseudo-second order evaluation are shown in Figure 4.

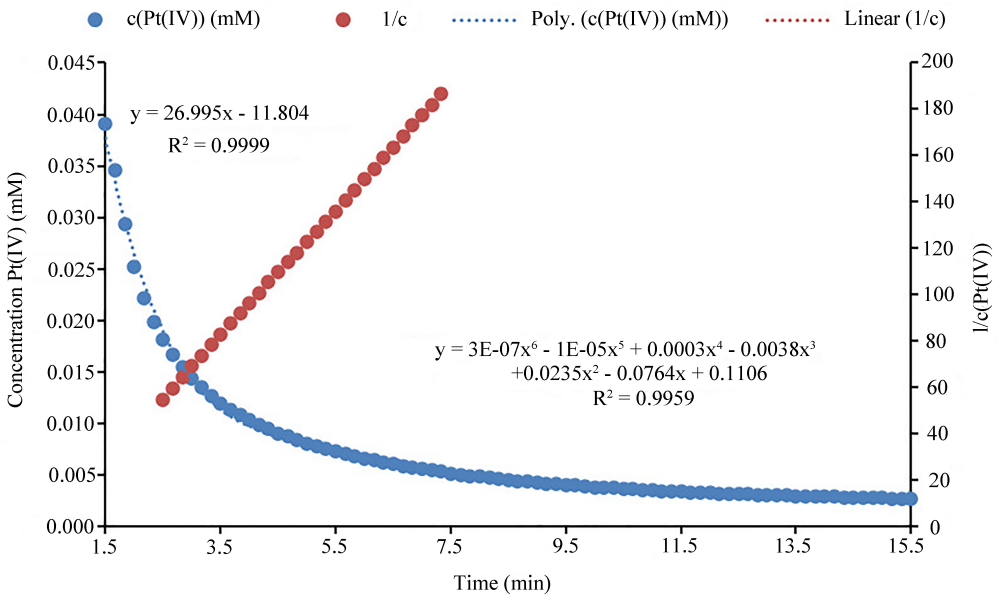

Figure 4. Kinetics of 0.04 mM K_2PtCl_6 with 100 mg GNP in DI with an empirical function (blue) and the pseudo-second order evaluation (red)

Kinetic data for the second (15 min, 0.04 mol L^{-1}) and third (30 min, 0.04 mmol L^{-1}) dosing are shown in Figure 5. The reaction can be fitted from 20.5–27.5 min and from 36.0–58.0 min to pseudo-second order kinetics with rate constants of k_{obs} 5.14 ± 0.05 M^{-1} min^{-1} and k_{obs} 1.84 ± 0.01 M^{-1} min^{-1} (Table 5).

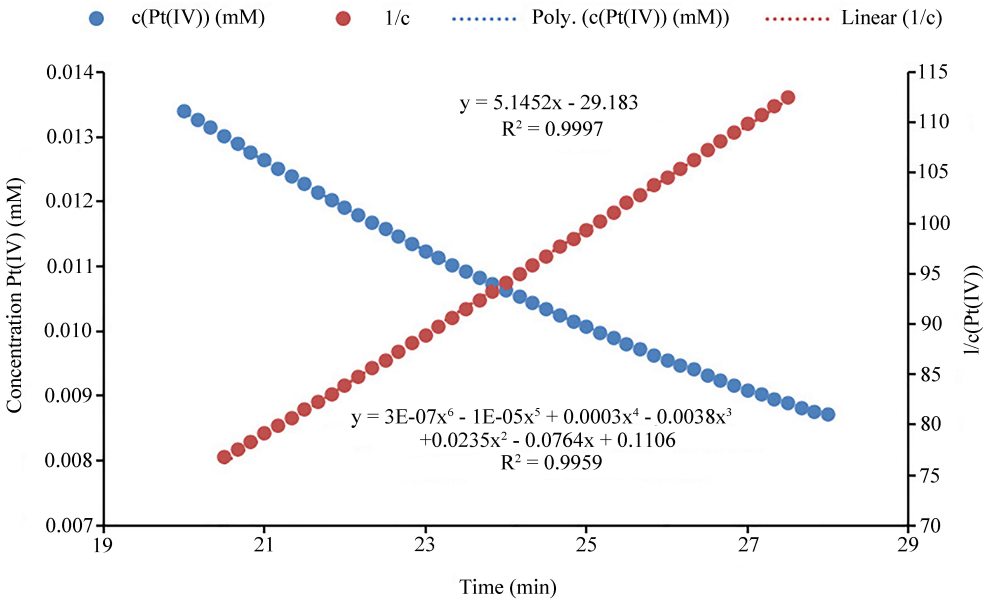

(A)

Figure 5. *Cont.*

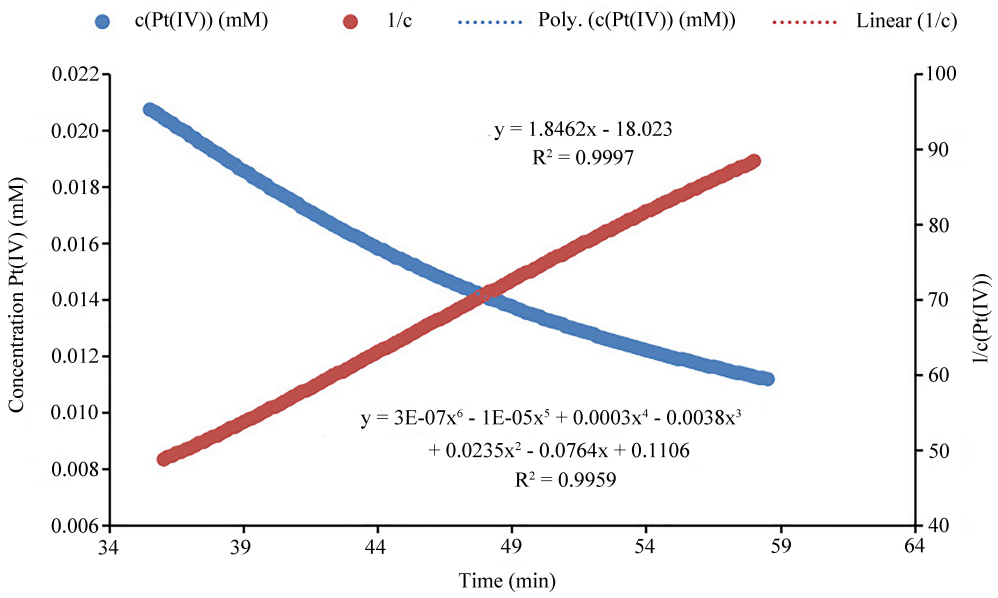

(B)

Figure 5. Kinetics of second (**A**) and third dosage (**B**) of 0.04 mM K_2PtCl_6 with 100 mg GNP with an empirical function (blue) and the pseudo-second order evaluation (red)

After 24 h, the Pt-GNP nanocomposite was isolated and analyzed with STEM and XPS (Section 3.4.3).

3.2.4 *Kinetics of Pd (II) with GNP*

Since 0.4 mM ammonium tetrachloropalladate (II) was not stable to hydrolysis[66], it was reacted with 500 mg GNP in acidic solution (10 mM HCl). The reaction with GNP can be evaluated from 3.82–4.20 min with a pseudo-second order kinetics (Equation (4)) and a rate constant of k_{obs} 8.1 ± 0.1 M^{-1} min^{-1} (Table 5). The time-dependent decrease of Pd (II) and the pseudo-second order evaluation are shown in Figure 6A.

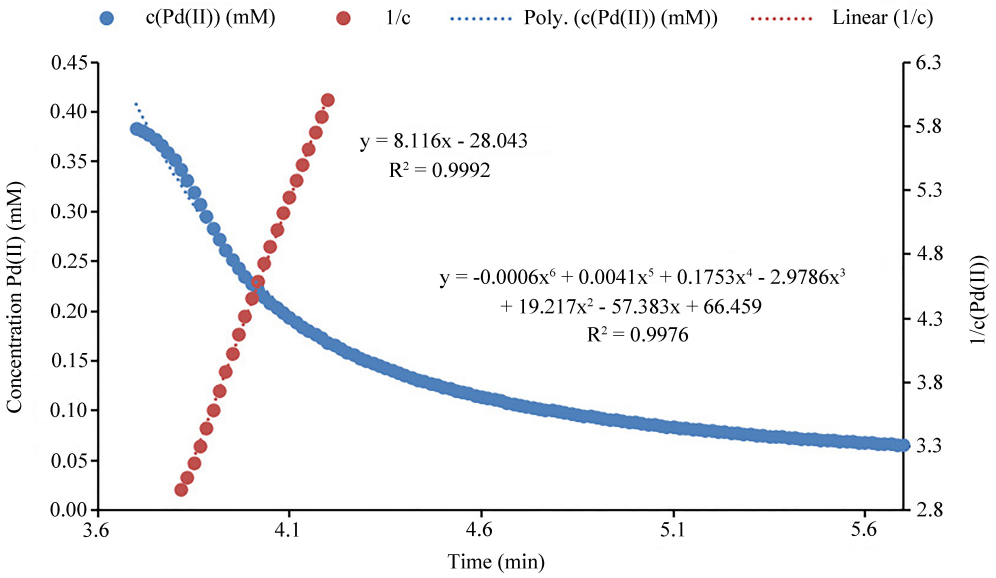

(A)

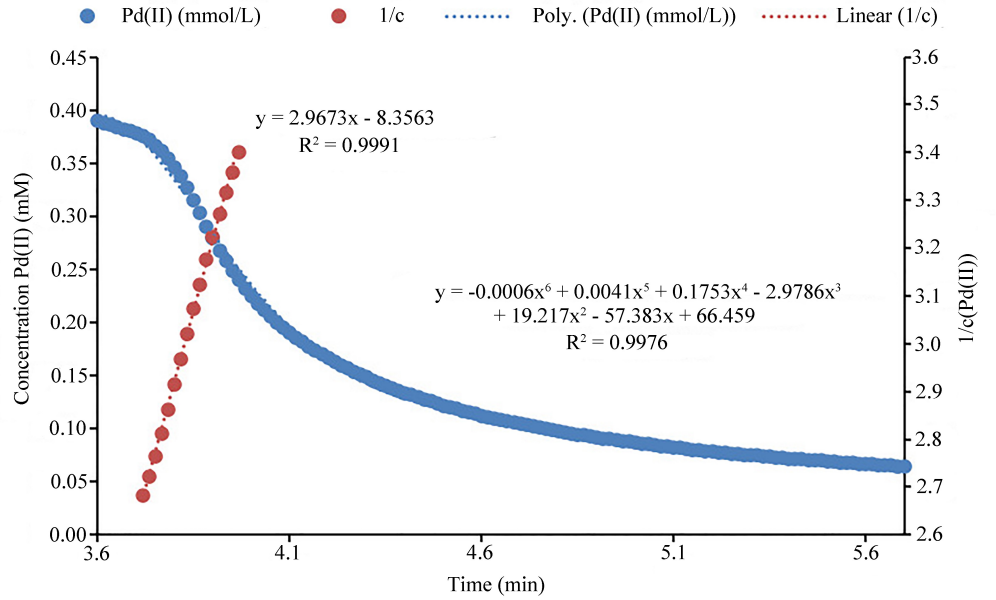

(B)

Figure 6. Kinetics of 0.4 mM $(NH_4)_2PdCl_4$ in 10 mM HCl with (**A**) 500 mg GNP with an empirical function (blue) and pseudo-second order evaluation (red); (**B**) with 500 mg GNP reg with an empirical function (blue) and pseudo-second order evaluation (red)

After 24 h, the Pd-GNP nanocomposite was isolated and analyzed by STEM and XPS (Section 3.4.4). Under otherwise identical conditions, GNP reg and Pd (II) reacted with pseudo-second order kinetics (Table 5). The reaction is best evaluated between 3.72 and 3.97 min with a rate constant of k_{obs} 2.97 ± 0.05 M^{-1} min^{-1} (Figure 6B). Thus, the use of thermally regenerated GNP resulted in a reduction of the rate constant by a factor of 2.9.

3.3 *Redox potential measurement of oxometalate solutions*

In redox reactions, the magnitude of the driving force, represented by the Gibbs free energy, which is proportional to the redox potential differences between the metal ion and the GNP, determines the position of equilibrium, i.e., the degree of occupation of the GNP according to Equation (5). Since the GNP represents a heterogeneous phase and Equation (5) can only be applied in a homogeneous phase, in this case the relative potential change (E_{ox}) caused by the noble metal ions in the aqueous phase was determined.

$$\Delta G^0 = -n \times F \times (E_{red} - E_{ox}) \quad (5)$$

The influence of 0.04 mM noble metal ions on the oxidation reduction potential (ORP) was measured in air-saturated AW and for Pd (II) in 10 mM HCl and the ORP shift due to oxometalate dosage was calculated as the difference between the mean before and after addition (Table 6).

Table 6. ORP of noble metal salts in water.

Substance	Concentration (mM)	Mean ORP before Dosage (mV) [1]	Mean ORP after Dosage (mV) [1]	ORP Metal Ion (mV) [2]
$(NH_4)_2IrCl_6$	0.04	219.5 ± 1.0	727.3 ± 0.5	507.8 ± 1.5
$HauCl_4$	0.04	227.1 ± 1.2	528.2 ± 0.1	301.2 ± 1.3
K_2PtCl_6	0.04	285.1 ± 0.4	427.2 ± 1.2	142.1 ± 1.6
$(NH_4)_2PdCl_4$	10 (in 10 mM HCl)	531.2 ± 0.5	598.6 ± 0.6	67.4 ± 1.1

[1] Mean of 4 measurements with standard deviation; [2] differences between ORP after and before dosage

The ORP increased in the order Pd (II) < Pt (IV) < Au (III) < Ir (IV). The respective standard electrode potentials differ slightly, but are measured under standard conditions: $AuCl_4^-$/Au (0), E_0 = 1.002 $V_{/SHE}$ and $AuCl_2^-$/Au (0), E_0 = 0.926 $V_{/SHE}$ [72], $PtCl_6^{2-}$/Pt (0), E_0 = 0.72 $V_{/SHE}$ [73], $IrCl_6^{2-}$/$IrCl_6^{3-}$, E_0 = 0.899 $V_{/SHE}$ [74] and $PdCl_4^{2-}$/Pd(0), E_0 = 0.91 $V_{/SHE}$ [75].

3.4 *Characterization of noble metal species on GNP*

To obtain information about the noble metal/GNP nanocomposites, the products were analyzed by scanning transmission electron microscopy (STEM) and X-ray photoelectron spectroscopy (XPS) [76]. STEM reveals the morphology of a graphene sample and the nanostructures can be analyzed under optimal conditions with a resolution down to 0.1 nm. High-angle annular dark field (HAADF) was used to enhance the contrast. In HAADF, the image intensity is proportional to $Z^{1.6}$, where Z is the atomic number, thus enhancing the contrast of single heavy element atoms on the carbon support. Combining bright and dark field images can lead to better detection of lighter and heavier atoms. Energy dispersive spectroscopy (EDS) provides information about the elements present and their proportion in the analyzed area. In addition, the element distribution can be mapped. XPS detects chemical species through a photoelectric effect under X-ray stimulation. This provides data on the composition of elements in the surface. High-resolution XP spectra provide information about the oxidation state and binding status of the elements. Both methods, STEM and XPS provide valuable information about element concentrations of noble metal elements when higher than 0.1 atom% or 0.5 mass% [77,78].

3.4.1 *Gold covered GNP*

The product of the reaction of Au (III) with GNP according to Section 3.2.1 (Au-GNP) was isolated and analyzed with XPS (Table 7). HR-XPS revealed the coverage of GNP with elemental gold, but also Au (I) and Au (III) in the percent range. Due to the small amount of the oxidized gold species Au (I) and Au (III), the quantification is difficult and associated with an increased error of up to ±2% [79,80]. The enhanced oxygen content of Au-GNP nanocomposites is discussed in Section 4.

Table 7. Elemental concentrations of Au-GNP with XPS

Au-GNP	C (%)	O (%)	Au (%)	N (%)	Composition (%)		
Atom%	83	14.7	0.9	1.4	Au (0)	Au (I)	Au (III)
Mass%	69.8	16.5	12.4	1.4	94.2	3.8	1.9

The HR-STEM images of Au-GNP are shown in Figure 7. Brightfield STEM (Figure 7A) showed the hexagonal structure of the GNP with disordered zones (yellow circle). In the dark field image (Figure 7B), three single gold atoms and in an almost linear arrangement are visible as bright spots. By superimposing bright-field and darkfield images (Figure 7C), it is visible that gold atoms are mainly located in disordered graphene zones.

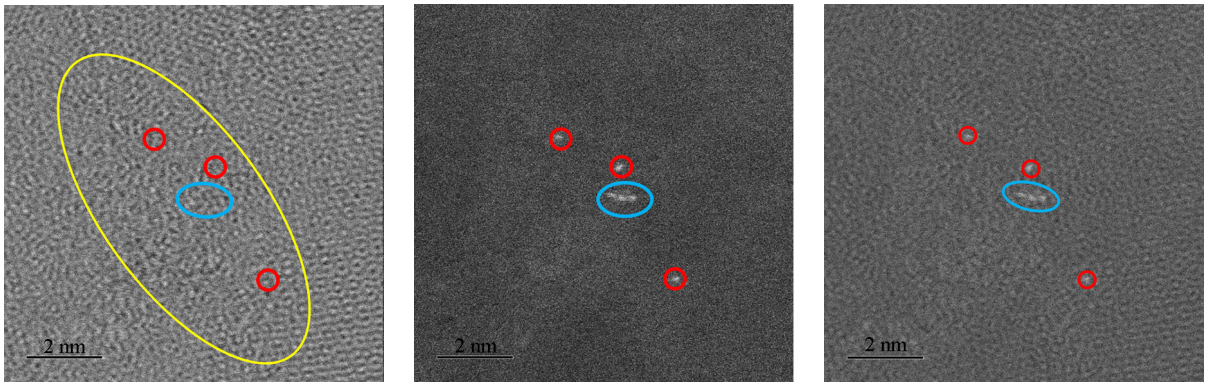

(A) (B) (C)

Figure 7. HR-STEM of gold atoms (red) and a small cluster (blue) on GNP; (**A**) STEM-BF, (**B**) HAADF; (**C**) Bright and dark field pictures superimposed; Disordered GNP zone (yellow)

If the reaction time for gold is extended to 14 days to saturation, a gold colored product is obtained. TEM was not performed due to high coverage. The elemental data of the XPS are given in Table 8. Silver was also found on the saturated Au-GNP. This was due to a contamination of 4.4 ppm silver in $AuCl_3$ according to the certificate of analysis, while the gold content was certified at 17.0%.

Table 8. Elemental concentrations of Au-GNP with XPS

Au-GNP, Saturated	C (%)	O (%)	Au (%)	N (%)	Ag (%)	Composition (%)		
Atom%	78.6	14.6	5.0	1.2	0.5	Au (0)	Au (I)	Au (III)
Mass%	42.3	10.5	44.1	0.8	2.4	94.7	3.3	2.0

An optical micrograph of the material is shown in Figure 8.

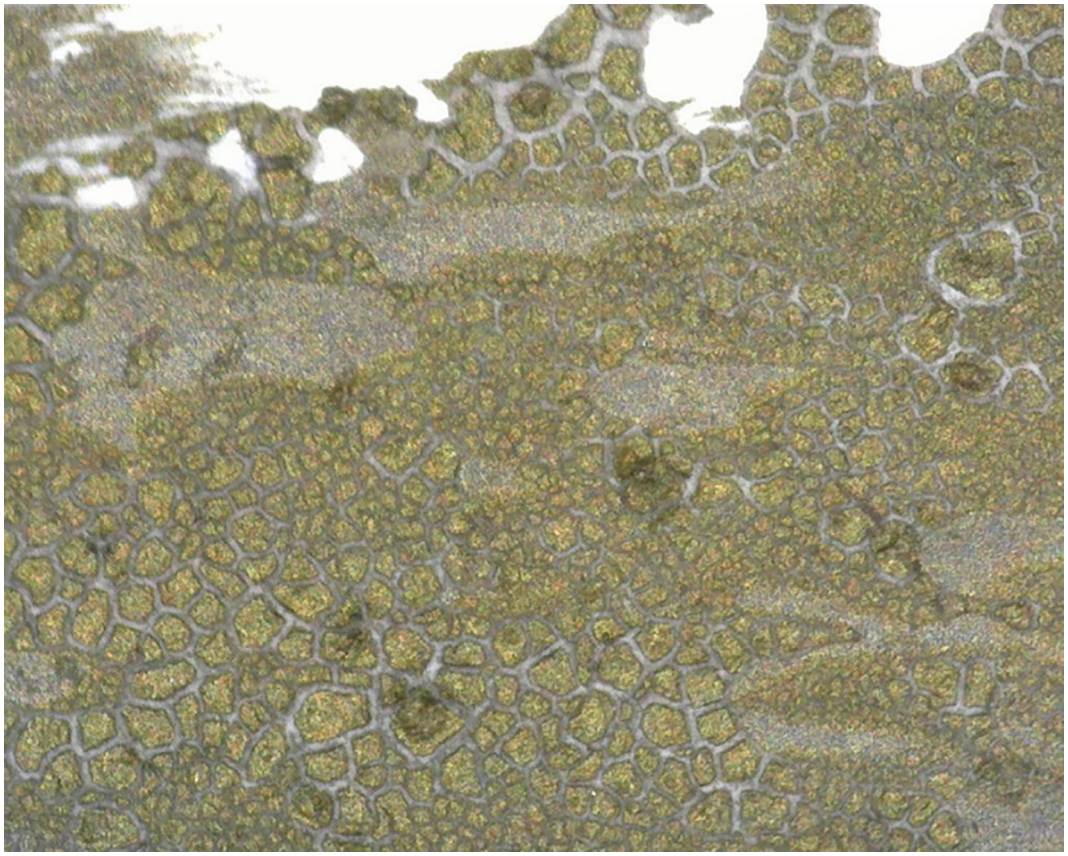

Figure 8. Optical micrograph of dried, saturated Au-GNP (reflected light, magnification: 80×)

3.4.2 *Iridium covered GNP*

The product of the reaction of Ir (IV) with GNP (Ir-GNP) according Section 3.2.2 was isolated and analyzed with XPS and STEM. The elemental composition with XPS is given in in Table 9.

Table 9. Elemental concentrations with XPS of Ir-GNP

Ir-GNP	C (%)	O (%)	Ir (%)	Cl (%)
Atom%	95.5	3.5	0.93	0.1
Mass%	82.6	4.0	12.9	0.3

The HR-XPS in Figure 9 shows that almost exclusively anhydrous and hydrated iridium dioxide were deposited on the surface in comparable portions[81]. The formation of the mixed-valent IrO_x can be ruled out, since an Ir 4f binding energy of 62.2 eV, known for Ir (III) ions, was not found[45]. The spectrum also indicates that no reduction of the metal to lower oxidation states has occurred.

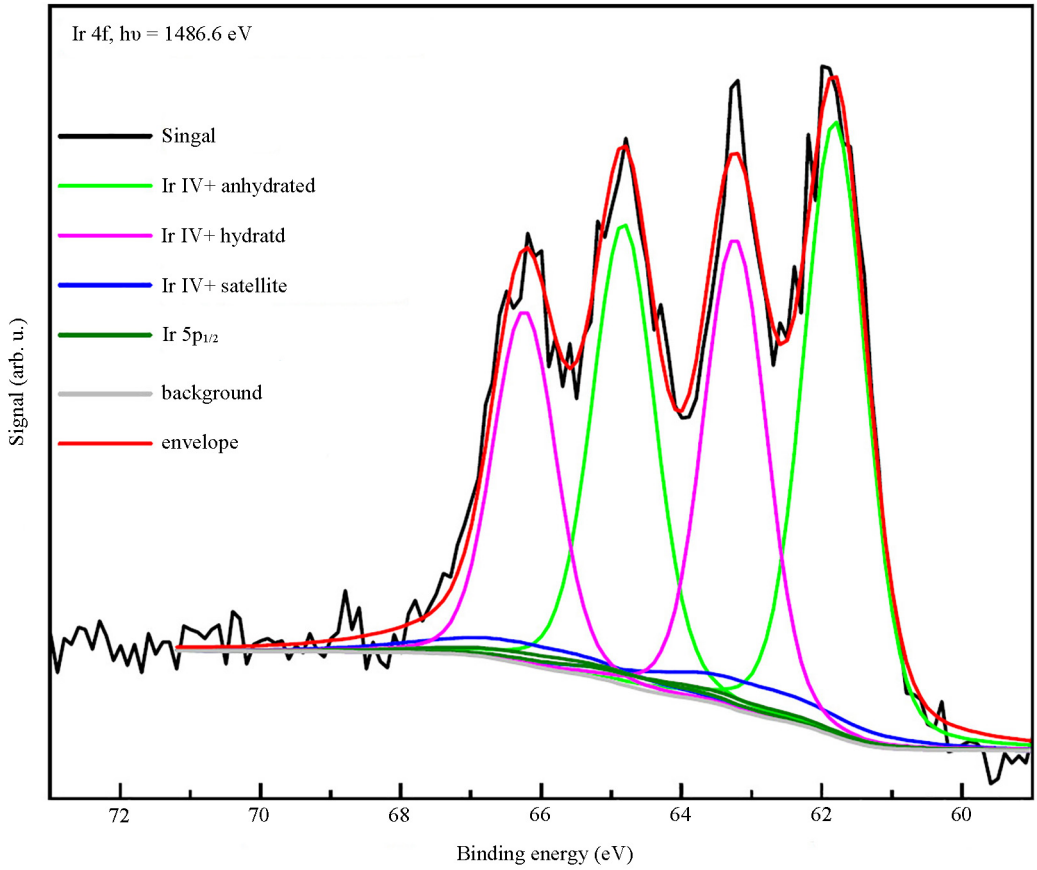

Figure 9. HR-XP spectrum of iridium (Ir 4f) on GNP

EDS elemental mapping of an Ir-GNP flake revealed a random distribution of carbon and iridium in Figure 10A. The magnification of Figure 10B shows structures <5 nm for the iridium species (Figure 10C).

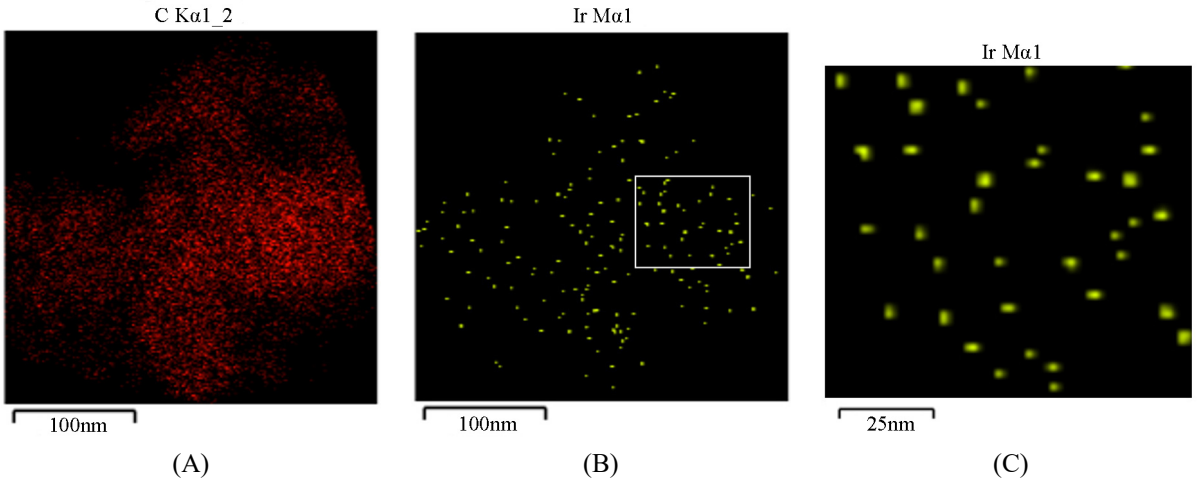

Figure 10. TEM-EDS element mapping of (**A**) carbon (C Kα1), (**B**) iridium (Ir Mα1) and (**C**) enlarged section of **B**

HR-STEM images (Figure 11) show single iridium atoms (red) and small clusters (blue).

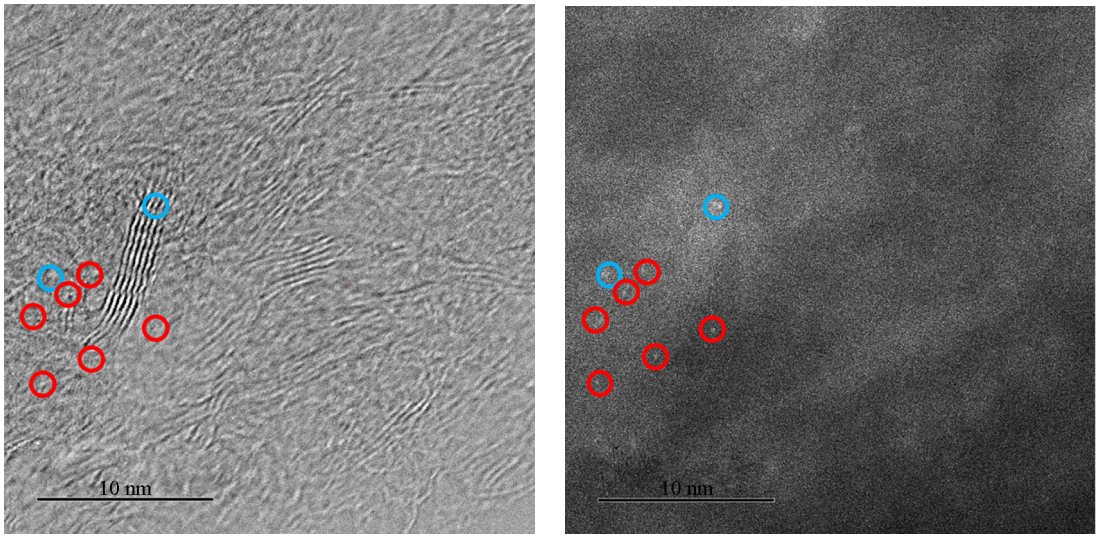

(A) (B)

Figure 11. STEM of iridium atoms (red) and small clusters (blue) on GNP; (**A**) STEM-BF, (**B**) HAADF

3.4.3 *Platinum covered GNP*

The reaction product of Pt (IV) with GNP (Pt-GNP), as described in Section 3.2.3, was isolated and analyzed by XPS and STEM. HR-XPS revealed the elemental composition and the distribution of Pt oxidation states (Table 10). The platinum was mainly present as Pt (II), while elemental platinum and Pt (IV) were present in the percentage range.

Table 10. Elemental concentrations with XPS of Pt-GNP

Pt-GNP	C (%)	O (%)	Pt (%)	Cl (%)	Composition (%)		
Atom%	92	6.7	0.3	0.5	Pt (0)	Pt (II)	Pt (IV)
Mass%	85.7	8.3	4.5	1.4	3.6	86.6	9.9

STEM-EDS revealed 97.7% carbon, 1.9% oxygen and 0.3% platinum, which is in good agreement with XPS. In contrast, HR-STEM was not successful due to problems with electron beam focusing. The reason was that a substance, probably hydrochloric acid, evaporated under the bombardment of electrons. Therefore, the Pt-GNP were modified with MESNA which is known to react with Pt (IV) complexes to form Pt (II)[61]. The elemental analysis of MESNA modified Pt-GNP by XPS is shown in Table 11.

Table 11. Elemental concentrations with XPS of Pt-GNP after reaction with MESNA

Pt-GNP (MESNA)	C (%)	O (%)	Pt (%)	Cl (%)	S(%)
Atom%	85.5	13	0.3	0	1.2
Mass%	77.1	15.6	4.4	0.0	2.9

No chlorine was found above 0.1 atom%, but 1.2 atom% sulfur. The ratio of platinum to sulfur was 1:4. TEM-EDS elemental mapping revealed the distribution of carbon and platinum atoms (Figure 12). For platinum, it resembles a random distribution with no recognizable structures at the nanometer scale.

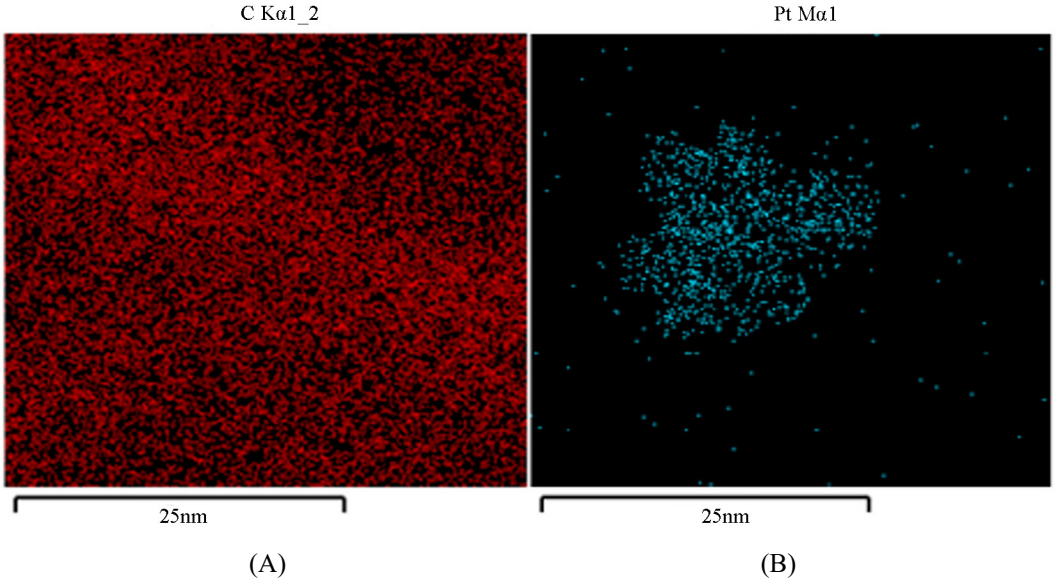

Figure 12. STEM-EDS element mapping of (**A**) carbon (C Kα1) and (**B**) for platinum (Pt Mα1)

After derivatization, the HR-STEM could be measured without any problems. It showed small and medium-sized platinum clusters shielded by MESNA or the reaction product (DIMESNA) (Figure 13).

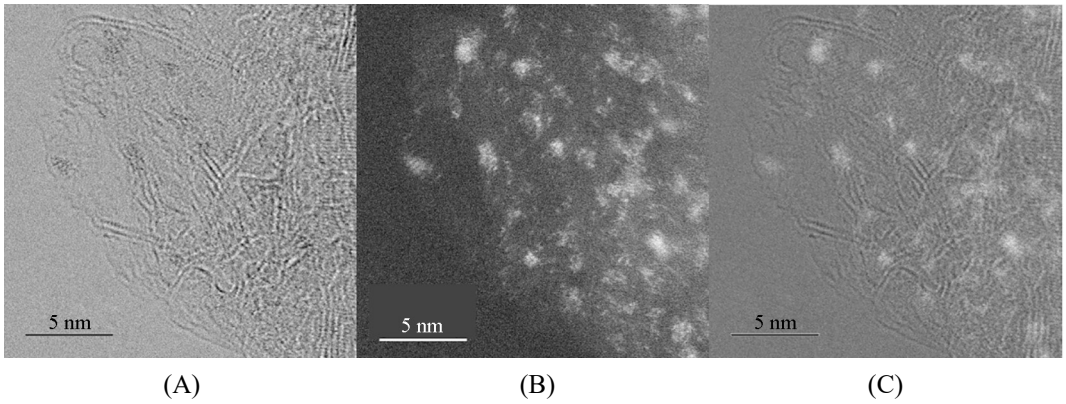

Figure 13. STEM of platinum clusters on GNP; (**A**) STEM-BF, (**B**) HAADF; (**C**) Bright and dark field pictures superimposed

3.4.4 *Palladium covered GNP*

The product of the reaction of Pd (II) with GNP according Section 3.2.4 (Pd-GNP) was isolated and analyzed with XPS and STEM. The elemental composition with XPS is given in Table 12.

Table 12. Elemental concentrations with XPS of Pd-GNP

Pd-GNP	C (%)	O (%)	Pd (%)	S (%)
Atom%	91.5	8.2	0.22	0.1
Mass%	86.1	10.3	3.3	0.3

Due to the low palladium concentration, the HR-XP spectrum is noisy (Figure 14). Nevertheless, it can be deduced that ~55% of the palladium is present as Pd (II), probably as palladium (II) oxide, and ~40% as metallic palladium, although an error of at least ±5% has to be considered. The binding energies of 337.48 and 342.77 eV can be attributed to PdO $3d_{5/2}$ and $3d_{3/2}$ split orbitals[82], while the binding energies of 335.19 and 340.48 eV can be assigned to Pd (0)[3].

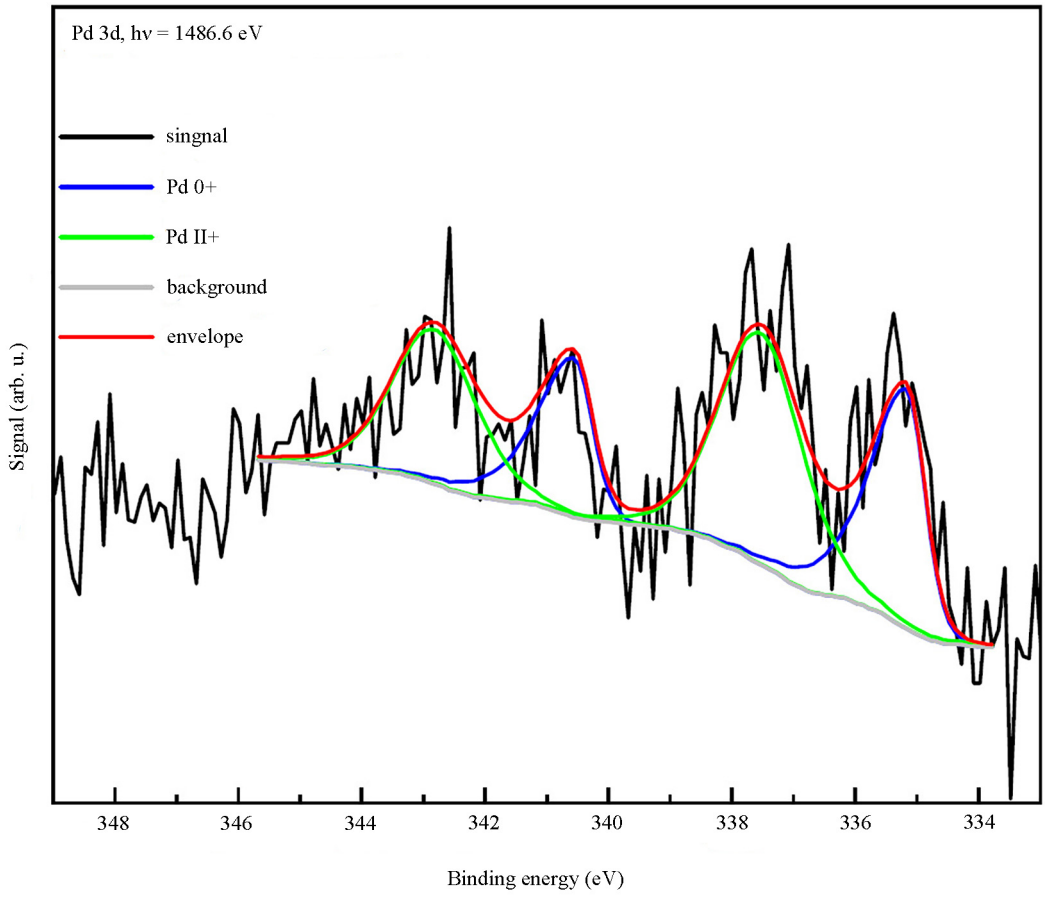

Figure 14. HR-XP spectrum of palladium (Pd 3d) on GNP

Elemental mapping of a GNP flake revealed a random distribution of carbon and palladium atoms (Figure 15) with no detectable structure at the nanometer scale.

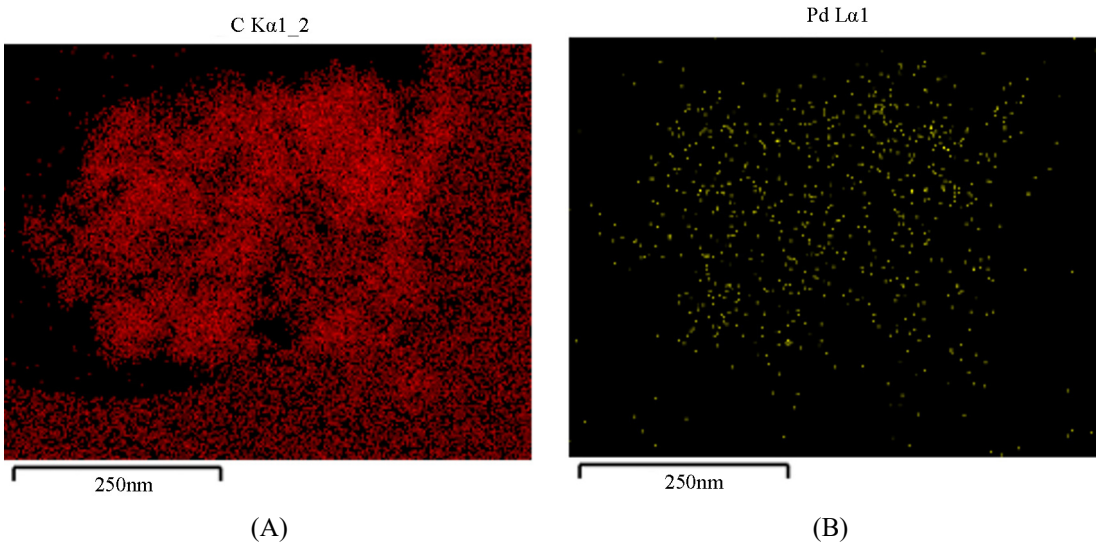

Figure 15. STEM-EDS element mapping of (**A**) carbon (C Kα1) and (**B**) palladium (Pd Lα1)

HR-STEM images (Figure 16) show single palladium atoms (red circles), small clusters (blue circles), and some medium-sized clusters (yellow circles).

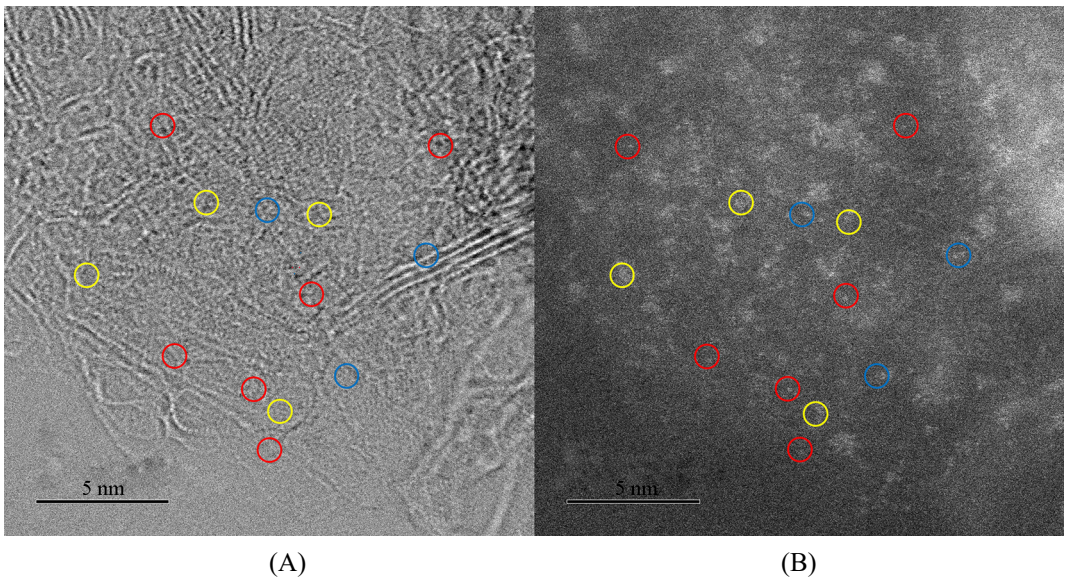

Figure 16. STEM of palladium atoms and clusters on GNP; (**A**) STEM-BF, (**B**) HAADF

4. Discussion

Graphene nanoplatelets with a high specific surface area reacted with chlorocomplexes of gold (III), platinum (IV), and palladium (II) in air-saturated water. The products were GNP nanocomposites decorated with noble metals or their compounds in lower oxidation states. Depending on the element, single atoms, small clusters and, more rarely, medium-sized clusters were formed. In the case of tetrachloroiridate (IV), the reaction path to Ir-GNP is accompanied by a reduction

of hexachloroiridate (IV) to hexachloroiridate (III). A plot of GNP precious metal loading as a function of ORP is shown in Figure 17. The metal content increases with increasing ORP (Table 6) with an approximately linear correlation.

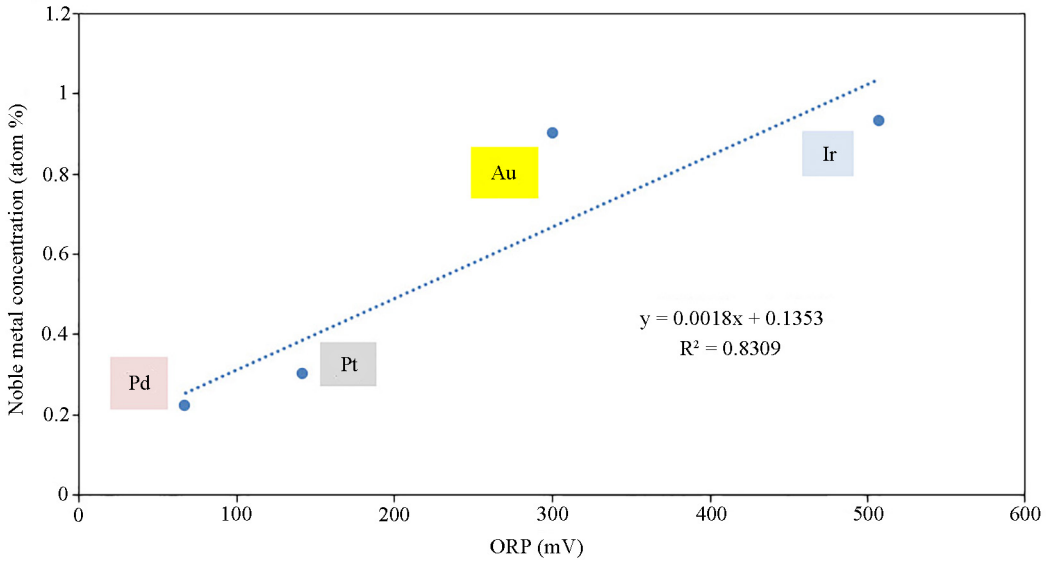

Figure 17. Noble metal concentration on GNP versus ORP

The main driving force of the reactions is the difference in redox potentials between the metal ion and the GNP, as given in Equation (5). For gold, the situation is special, as the reaction proceeds to a gold-colored material (Figure 8) with 44 mass% gold. A similar observation as with GNP was made with rGO, where the entire layers were covered with gold[79]. This may be due to the high affinity of Au (0) for carbon[3]. The metal ions with the highest redox potential, Au (III) and Ir (IV), reacted with pseudo-first order kinetics. This is comparable to the reaction of potassium permanganate with GNP, where pseudo-first order kinetics were also found with an ORP for Mn (VII) of 506.5 ± 2.3 mV[20]. While the GNP contained 8.9 mass per cent oxygen, the oxygen content in the Au-GNP was increased to 16.5 mass per cent, so that the difference of 7.6% is significant, while the other metal-GNP nanocomposites did not show such a strong increase. In an earlier study, potassium permanganate was reacted with GNP and yielded comparable values: at a manganese loading of 30 mass% (10 atom%), an oxygen content of 23.8 mass% was found[20]. This similarity and the pseudo-first order kinetics for both metal ions suggest a common mechanism leading to high oxygen incorporation in the nanocomposites. A density functional theory (DFT) calculation[80] predicted a cyclic reaction intermediate for the reaction of graphene with permanganate, which fits the pseudo-first order reaction if the observed rate constant represents an elementary reaction. Here, two adjacent carbon atoms are oxidized by a permanganate ion, which after hydrolysis leads to hydroxyl groups and further to defects on the upper graphene layer. For the reaction of Au (III) with graphene, we are not aware of any corresponding DFT studies on the reaction intermediates, but oxidation of graphene layers must take place. A catalytic process is also possible: molecular oxygen was present in the reaction medium (~9 mg/L at 20 °C) and is known to adsorb on GNP with pseudo-second order absorption kinetics according to Equation (2)[20]. In the absence of Au-GNP, the process is slow with a rate constant k_{PSO} of ~0.50 mM^{-1} min^{-1}. Au-GNPs are known to be good oxidation catalysts[3,84].

The reaction of 0.04 mM Au (III) with GNP had a halftime ($\tau_{1/2}$ exp) of 0.5 min (Table 3), and the decrease in Au (III) concentration is best evaluated with pseudo-first order kinetics (Table 5). In contrast, pseudo-second order kinetics were found for the adsorption of Au (III) on GO, which result in a product with ~10 mass% Au[31]. For comparison, the sorption of gold (III) on activated carbon follows pseudo-first order kinetics and Au (0) is the main product[85,86]. Surface phenolic groups have been identified as reducing agents. With 0.5 mM Au (III), which is about 12.5 times higher than in this study, gold microparticles in the range of 1 to 10 μm were formed. The gold content was low at 0.11 atom%, and

the composition of oxidation states was 89.8% Au (0) and 10.2% Au (III), while no Au (I) was present[86]. In 2012, it was shown that rGO reacts with auric acid in water without reducing agents to form a nanocomposite with an Au content of 1.8–7.2 atom%, depending on the auric acid concentration (0.5–2 mM) and the reaction time[32]. Using STEM, gold nanoparticles with an average size of 1.8 ± 0.2 nm were identified on the rGO, and using XPS, mainly Au (0) was found. In a recent study, ultrasonically generated GNP were reacted with 1, 5, and 10 mol% gold (III) acetate, resulting in gold nanoparticles with average sizes of 8.3, 29.7, and 32.1 nm on the GNP. The alternative precursor tetrachloroauric acid yielded gold nanoparticles with an average size of 1.8 nm at a concentration of 1 mol%[35]. Unfortunately, this material was not tested further. The concentration of GNP was 0.1 mg/L, which is lower than in this study (0.4 mg/L) and should be advantageous. However, the gold salts were added in solid form, which creates a high local Au (III) concentration and is not conducive to the formation of gold atoms or small clusters. Mixing was done for one minute, no stirring is mentioned. The nanocomposites were studied in detail, but no kinetic data were collected. The fractions of the oxidation state ratios were Au (0) 84.17%, Au (I) 4.46%, and Au (III) 11.38%[35]. In this study, the oxidation state fractions were distributed as 94.2% Au (0), 3.8% Au (I) and 1.9% Au (III) at a loading of 0.5 atom% gold (Table 7). This indicates that the reduction capacity of the ultrasound-generated GNP was lower than that of the xGNP® used here. A higher coverage of the GNP of up to 5.0 atom% (44.1 mass%) was accessible through longer reaction times (Table 8). The ratio of the oxidation states Au (0):Au (I):Au (III) shifted only slightly with increasing occupancy to 94.7:3.3:2.0. There are three clear differences to the experiments described here: 1. The group used rGO instead of GNP, 2. The concentration of the metal ion solution was 12 times higher than in this study (0.5 mM, here 0.04 mM), 3. The initial ratio of metal to rGO mass was higher with 2.94 $\times 10^{-3}$ mmol mg^{-1} compared to GNP with 4.0 $\times 10^{-5}$ mol mg^{-1} and 4. The product in this case was gold nanoparticles with >1 nm. Instead, single gold atoms and small clusters of three atoms with an almost linear arrangement were found in this study (Figure 7). The study[32] successfully demonstrated the suitability of gold nanocomposites for ORR catalysis. For electrode modification, the decoration of graphene films using $AuCl_3$ wet coating process has been reported previously. A 5 mM $AuCl_3$ solution was used and after 20 s of immersion, the surface potential of graphene films can be adjusted up to 0.5 eV by controlling the immersion time[87]. In another study, the improvement of graphene LED electrodes by p-doping was achieved by immersing the graphene electrodes in 5, 10 and 20 mM $AuCl_3$ solutions[88]. It should be noted that in these cases the Au (III) concentration was a factor 125 times higher than in the case reported here.

According to a combined experimental and DFT study, the apparent linear arrangement of three gold atoms as seen in the HR-TEM in Figure 7 is not stable, but the triangle and the contact to the graphene is made by a single Au atom. Small gold clusters and sub-nanometer clusters with Au_3 and Au_6 clusters were found to be stable on a graphene field effect transistor[89]. This confirmed the results of a previous study that investigated the adsorption of Au_1 to Au_4 gold clusters on graphene, focusing on electronic structure analysis[90]. A further, extensive DFT study revealed the most stable orientation, adsorption site, adsorption energy and diffusion barrier of 30 metal adatoms on graphene. For gold adatoms on pristine graphene, the position on a tertiary carbon atom is favored with an adsorption energy of 0.11 eV[91]. Gold was deposited on a graphene layer at 18 K under ultra-high vacuum (UHV) conditions, where the single atoms and small clusters showed no mobility. Between 18 K and 210 K, the measured mobility was increased by a factor of three[92]. Increasing the temperature favored the formation of clusters, as demonstrated by atomic force microscopy. This is consistent with an ab initio DFT study with van der Waals corrections combined with electron microscopy data, which showed that gold atoms have a low migration barrier, indicating high mobility at 300 K. STEM of gold on multilayer graphene revealed that gold prefers the positions at the edges of the layers. The results suggest that the single Au atoms found in this work were stabilized by graphene defects, especially at the sheet edges[93]. An example of the strong interaction of Au atoms with graphene edges was filmed, showing that the embedded Au atom can be moved between energy favorable positions under STEM electron beam conditions[94].

The sorption of 0.2 mM Ir (IV) with GNP had a $\tau_{1/2}$ exp of 0.3 min (Table 3), and the decrease in Ir (IV) concentration is best evaluated with a pseudo-first order rate constant (Table 5). Two Ir (IV) doses within 30 min resulted in iridium saturated GNP. The maximum loading was high at 0.93 atom% (12.9 mass%) iridium (Table 9), but significantly lower than for gold. According to HR-XPS, iridium (IV) is deposited on the GNP as anhydrous and hydrated iridium (IV) oxide (Figure 9), while no mixed-valence IrO_x[45] or metallic iridium was found. Formally, the sorption is not a redox reaction, but rather a solvolysis, although the hydrolytic stability of Ir (IV)-chlorine complexes under the applied conditions and

the rapid sorption of Ir (IV) suggest a reaction. According to the literature[95], a reduction to oligomeric mixed Ir (III) di-μ-oxo-bridged hydroxides could have occurred, as it was found in the anodic regime on iridium electrodes for the OER. A subsequent oxidation reaction with the oxygen dissolved in the water may have produced hydrated iridium (IV) clusters that retain the linear structure. STEM-EDS showed a random distribution of Ir species (Figure 10), while HR-STEM showed single Ir atoms, which are more likely to be IrO_2 molecules and clusters of anhydrous and hydrated iridium dioxide (Figure 11). These species could also explain the linear atomic columns in STEM-EDS. According to[95], anhydrous rutile-type iridium (IV) oxide which was inactive in OER, can be formed in a side reaction. Anhydrous IrO_2 was also confirmed by HR-XPS in this study (Figure 9). Currently, nano-sized Ir (IV) oxide is being intensively investigated as an electrocatalyst[96]. The fact that GNP are reducing agents was demonstrated by the redox reaction of Ir (IV) with GNP via a second reaction channel, leading to a solvated hexachloroiridate (III) complex[64].

For platinum (IV) and palladium (II), the reactions with GNP were found to be pseudo-second order as with potassium chromate[20]. The ORP of 0.04 mM Cr (VI) was measured at 68.5 mV, which is comparable to 10 mM Pd (II) at 67.4 mV (Table 6), resulting in similar coverage for Cr and Pd. The reaction of 0.04 mM Pt (IV) with GNP had a $\tau_{1/2}$ exp of 0.5 min for the first dose (Table 3), while a total of three doses of 0.04 mM Pt (IV) were applied over a period of 60 min to saturate 100 mg GNP with platinum. The observed pseudo-second order rate constants decreased from the 1st to the 3rd dose, which is expected since the reactive sites on the GNP decreased due to the coating with platinum (Table 5). The maximum coverage of GNP was found to be 0.3 atom% (4.5 mass%) Pt. As for gold, the platinum was anchored on GNP in the three oxidation states: 3.6% Pt (0), 86.6% Pt (II) and 9.9% Pt (IV) (Table 10). In contrast to gold, where the metallic form predominated, the Pt (IV) was essentially reduced to Pt (II). For comparison, Pt (IV) reacted with activated carbon in acidic media according to pseudo-first order kinetics and the loading was low (0.08 atom% Pt), with oxidation states fractions of 47% Pt (II) and 53% Pt (IV)[97]. Sorption of Pt (IV) on rGO was only successful when sodium borohydride was used as an additional reducing agent, resulting in platinum nanoparticles with an average diameter of 1.9 nm on rGO[32]. This is due to the lower reduction potential of rGO compared to GNP. The adsorption kinetics with GO was described as pseudo-second order and resulted in a product with ~7 mass% Pt[32]. Pt-GNP in this work were not stable due to electron bombardment in HR-STEM as a volatile substance, e.g., hydrogen chloride, was released. Therefore, the chemical modification for the Pt species was demonstrated. MESNA, which is known to reduce square Pt (IV) complexes to Pt (II), was selected according to Equation (6) to form MESNA disulfide (DIMESNA)[61]. In excess of MESNA, a ion exchange with chloride and complexation with Pt (II) is likely. XPS shows that DIMESNA was adsorbed on the GNP with a Pt:S ratio of 1:4.0 (Table 11). This means that one molecule of DIMESNA or two molecules of MESNA were bound to GNP per platinum atom.

$$[PtCl_6]^{2-} + 2HSCH_2CH_2SO_3H \rightarrow [PtCl_4]^{2-} + HO_3SCH_2CH_2SSCH_2CH_2SO_3H + 2HCl \quad (6)$$

According to STEM-EDS, the platinum was randomly distributed on the GNP (Figure 12). HR-STEM showed small and medium-sized clusters (Figure 13) which were shielded by MESNA or DIMESNA. The presence of different oxidation states in principle allows the manipulation of each oxidation state by appropriate complexation or reaction, thus broadening the application of SACs[11,44,59].

A study combining DFT and bond-order potential calculations provided information on the adsorption energetics, structural features, and electronic structure of platinum nanoclusters supported on both defective and defect-free graphene. Platinum clusters exhibited low-symmetry shapes similar to those at point defects in the graphene plane and at edge anchor groups. The formation of metal-carbon bonds at support defects affects the bond length and strain in the metal cluster, and stronger binding correlates with larger bond lengths. In addition, stronger binding of the cluster to the support leads to increased charge transfer from the cluster to the substrate[98]. The dynamics of Pt_1 to Pt_{10} cluster growth on different graphene substrates with vacancies was investigated by DFT. Calculations showed that Pt clusters bind more strongly as the vacancy size increases. For a given vacancy size, increasing the cluster size leads to more endothermic formation energy, which limits cluster growth. For pristine graphene, the energy of formation becomes more exothermic with increasing cluster size. Again, platinum atoms on perfect and defective graphene sheets show asymmetric cluster growth on only one side of the support. Calculations showed that oxidation of the defect weakens the binding of the Pt cluster,

suggesting that oxygen-free graphene supports are critical for successful attachment of Pt to carbon-based substrates. Once the nanostructure is formed, oxygen adsorption is more favorable on the cluster than on the support[99]. A DFT study of Pt_n clusters with $n \leq 13$ revealed that the sorption of single Pt atoms and Pt dimers is favored by docking at bridges between neighboring carbon atoms. For small clusters, a vertical planar arrangement is more stable than a parallel planar or 3-dimensional arrangement due to the stronger graphene interaction. As the number of cluster atoms increases, the Pt-C interaction energy per contacting Pt atom decreases[100]. For Pt_n clusters with n ranging from 4 to 27, a DFT study showed that all clusters interact with the substrates through a single platinum atom, with adsorption at the bridging site being the most stable; the adsorption energy of the Pt_n clusters decreased uniformly as the number of platinum atoms increased[101]. Platinum dimers on rGO were synthesized by a bottom-up approach, which could be detected by STEM, where they showed Pt-Pt distance of 0.30 ± 0.02 nm. For use as a catalyst in hydrolysis reaction, scanning transmission electron microscopy, X-ray absorption spectroscopy and DFT calculations suggested that the Pt dimers are likely to exist in oxidized form, e.g., Pt_2O_x[102]. This could also be the case for the small clusters found in this study, since they were synthesized in air-saturated water.

In contrast to the other metals, 0.4 mM palladium (II) was reacted with 500 mg GNP in acidic solution to prevent hydrolysis[66]. The reaction had a $\tau_{1/2}$ exp. of 0.75 min and can be evaluated with pseudo-second order kinetics (Table 5). The ORP of Pd (II) measured in 10 mM HCl was 67.4 mV, the lowest of the four noble metals studied. A dosage of 0.4 mM Pd (II) resulted in the lowest coverage of 0.22 atom% (3.3 mass%) Pd (Table 12). HR-XPS (Figure 14) indicates the formation of ~55% palladium (II) oxide and ~40% metallic palladium. For comparison, an activated carbon was coated with 4.24 mass% Pd and the product was identified as $PdCl_2$, while no reduction of Pd (II) to Pd (0) occurred[103]. The kinetics are described with an adsorption equilibrium for the tetrachloropalladate (II) with $PdCl_2$ followed by the sorption of the poorly soluble $PdCl_2$[104]. The adsorption of Pd (II) on GO was evaluated with a pseudo-second order law and resulted in a material with ~8 mass% Pd, which may be due to the high functional group content in GO[34]. In this study, formal hydrolysis of the tetrachloropalladate (II) complex resulted in the formation of palladium (II) oxide. It seems possible that a redox reaction is involved in the formation of PdO, as in the case of Ir (IV), since tetrachloropalladate (II) is stable to hydrolysis under the conditions used (10 mM HCl) and a reduction product with metallic palladium was formed. When rGO is reacted with sodium tetrachloropalladate (II) and then subjected to a hydrothermal reaction at a temperature of 200 °C, a PdO network is formed on the GO[49]. It has been reported that rGO react with tetrachloropalladate without additional reductant to palladium nanoparticles with a size of about 1.4 nm[31]. In this study, STEM-EDS elemental mapping revealed randomly distributed palladium (Figure 15), while HR-STEM imaged predominantly single atoms and small clusters in addition to a few medium-sized clusters (Figure 15).

DFT calculations of palladium adsorbed on graphene were performed. One result was that palladium atoms deposited on graphene have a strong tendency to form clusters, with three-dimensional clusters being more stable than planar ones, and that a strong Pd-Pd interaction is also relevant starting with Pd_4[105]. A DFT study has been performed to evaluate the influence of graphene monovacancies on palladium clusters for hydrogenation. The large binding energy of small Pd_n clusters with n = 1 to 4 on these vacancies results from a strong hybridization between the unsaturated carbon and the Pd atoms, and it indicates that anchoring avoids migration of Pd clusters on the graphene surface. Pd_4 clusters on graphene are calculated to have a capacity to chemisorb four molecules of hydrogen, which should be advantageous for hydrogenation and hydrogen storage[106].

Thermally regenerated GNP were tested as a support to increase metal coverage. It is known that during storage GNP react partly irreversibly with oxygen and adsorb trace organic substances from the air (e.g., hydrocarbons)[21]. Thermal regeneration leads to desorption, decarbonylation and decarboxylation. However, under otherwise identical conditions, the kinetics of Pd (II) resulted in a rate constant reduced by a factor of 2.7 and an occupancy reduced by a factor of 1.7. The reason for this is probably the reduction of defect structures during thermal regeneration, which in turn indicates their important function in binding the palladium. For palladium dimers on graphene, DFT calculations revealed that the minimum energy configuration is an orientation of Pd_2 parallel to the graphene layer, with two atoms each occupying the center of adjacent hexagonal rings. Small energy differences between the adsorption sites at low diffusion thresholds indicate high mobility of the dimers. In the calculations, the dimers cause a significant deformation of the graphene layer perpendicular to the plane[107].

Dispersion in aqueous solution is a complex process because water forms two hydrophobic layers on graphene [108]. The first layer is 0.5 nm above the graphene surface and the second layer is 0.5 nm away from the first layer. These must be overcome by dissolved ions in the water before they reach the graphene surface. In this study, we used aerated water with a low salinity or 10 mM HCl to aggregate the nanoplatelets into microparticles and enable at-line analysis. The presence of dissolved oxygen in the water should also not be neglected, as it adsorbs on GNP but does not seem to have a negative effect when a reaction takes place, as with oxometalates [20] or noble metal chlorometalates. The reactions of noble metal chlorometalates with GNP presented here are heterogeneous reactions that can be described by the "shrinking core" model, where the number of reactive sites decreases as the reaction progresses [109]. The kinetics are complex and consist of at least three steps, although the reduction of the metal ions follows simple rate laws obtained by holding the reaction conditions constant [20]. The first step is the diffusion of the chlorometalate from the bulk liquid to the GNP surface through the concentration boundary layers, the sorption on the surface or on an already reduced metal atom or cluster, followed by the reduction by the GNP, possibly mediated by the adatom. For a given surface, the mass transfer coefficient in the concentration boundary layer during adsorption or the rate constant during a reaction and the concentration of the reactant in the main liquid phase are decisive for the time-dependent mass transfer. Important factors that accelerate the kinetics are

- Increasing the surface area of the solid, here the GNP;
- Reduction of particle size, here nanoplatelets;
- Increasing the relative liquid/solid velocity, here achieved by stirring at 800 rpm.

In this respect, the process chosen here differs from the reduction of chlorometalates in solution to form clusters or nanoparticles with subsequent adsorption on the support, or from the sorption of chlorometalates on GO with subsequent reduction.

5. Summary and conclusions

Graphene nanoplatelets with a high specific surface area of 750 m^2 g^{-1} reacted with chlorocomplexes of gold (III) and platinum (IV) in air-saturated water or 10 mM hydrochloride solution as in the case of palladium (II) to form single atoms and clusters on GNP. HR-XPS was used to determine the elemental contents of the nanocomposites and the oxidation states of the metals; HR-STEM was used to determine the distribution and size of the metals on the GNP. For gold, single atoms and small clusters were found, mainly in the metallic state; for platinum, small and medium-sized clusters were found, mainly as Pt (II) besides metallic Pt and Pt (IV); for palladium atoms, small and some medium-sized clusters were detected, mainly consisting of palladium oxide (~55 atom %) and metallic palladium (~40 atom%). Iridium was deposited as clusters as iridium dioxide in the anhydrous and hydrated states. Soluble hexachloroiridate (III) was formed as a by-product. The noble metal content of the nanocomposites increased with the series: Pd (0.22 atom%), Pt (0.30 atom%), Ir (0.93 atom%) and Au (5.0 atom%). The driving force for the reaction of higher oxidation state chlorometalates with GNP is the potential difference between the graphene as reducing agent and the metal ion as oxidizing agent. Thus, the metal loading increases with the oxidation potential of the noble metal ion. If the reduced metal species are insoluble, they will be deposited on the GNP. Gold (III) and iridium (IV) with the higher ORP were best evaluated with pseudo-first order kinetics, while platinum (IV) and palladium (II) with the lower ORP followed a pseudo-second order law. The presence of different oxidation states has been documented for gold, platinum, and palladium, opening the possibility of specifically modifying the oxidation state [11,44,59]. This has been demonstrated for the reduction of platinum (IV) on GNP with MESNA. The behavior of GNP towards the chlorometalate complexes of the noble metals is clearly different from that of GO and finally rGO, which can be attributed to the decreasing reduction potential in the series GNP, rGO and GO. The GNP were suspended as microparticles in water with a certain salinity, which can be separated by filtration, and the sorption of the chlorometalates was monitored by at-line UV-Vis spectrometry at the specific LMCT wavelengths to obtain a kinetically controlled, defined noble metal loading. As a contribution to sustainability, the reaction media, with the exception of Ir (IV), can be recycled.

The metal-decorated graphene nanoplatelets are interesting materials to be tested as SACs in electrocatalysis [12], organic synthesis [110], and photochemistry [111]. It would be a significant advance to use industrially produced, widely available, and well-characterized materials as supports, which seems particularly important for graphene with its diverse synthetic routes [60].

Acknowledgments

The authors would like to thank the people who helped with this work. They also appreciate the valuable work and suggestions of the reviewers.

Conflict of interest

There is no conflict of interest for this study.

AI support

Google Translate and DeepL Write were used for Word processing of this article.

References

[1] Mitchell, S.; Pérez-Ramírez, J. Single atom catalysis: a decade of stunning progress and the promise for a bright future. *Nat. Commun.* **2020**, *11*, 1–3. https://doi.org/10.1038/s41467-020-18182-5.

[2] Luo, Z.; Castleman, A. W.; Khanna, S. N. Reactivity of Metal Clusters. *Chem. Rev.* **2016**, *116*, 14456–14492. https://doi.org/10.1021/acs.chemrev.6b00230.

[3] Kaiser, S. K.; Chen, Z.; Akl, D. F.; Mitchell, S.; Pérez-Ramírez, J. Single-Atom Catalysts across the Periodic Table. *Chem. Rev.* **2020**, *120*, 11703–11809. https://doi.org/10.1021/acs.chemrev.0c00576.

[4] Cheng, Y.; Wang, H.; Song, H.; Zhang, K.; Waterhouse, G. I.; Chang, J.; Tang, Z.; Lu, S. Design strategies towards transition metal single atom catalysts for the oxygen reduction reaction—A review. *Nano Res. Energy* **2023**, *2*, e9120082. https://doi.org/10.26599/nre.2023.9120082.

[5] de Bolster, M. W. G. Glossary of terms used in bioinorganic chemistry (IUPAC Recommendations 1997). *1997*, *69*, 1251–1304. https://doi.org/10.1351/pac199769061251.

[6] Berry, R. Stephen. "Cluster". Encyclopedia Britannica, 7 February 2019. Available online: https://www.britannica.com/science/cluster (accessed on 29 March 2024).

[7] Konradt, N.; Dillmann, S.; Becker, J.; Schroden, D.; Rohns, H.-P.; Wagner, C.; Müller, U.; Konradt, D.; Janknecht, P.; Hobby, R.; et al. Removal of Chromium Species from Low-Contaminated Raw Water by Different Drinking Water Treatment Processes. *Water* **2023**, *15*, 516. https://doi.org/10.3390/w15030516.

[8] Sabzehmeidani, M. M.; Mahnaee, S.; Ghaedi, M.; Heidari, H.; Roy, V. A. L. Carbon based materials: a review of adsorbents for inorganic and organic compounds. *Mater. Adv.* **2021**, *2*, 598–627. https://doi.org/10.1039/d0ma00087f.

[9] Han, L.; Cheng, H.; Liu, W.; Li, H.; Ou, P.; Lin, R.; Wang, H.-T.; Pao, C.-W.; Head, A. R.; Wang, C.-H.; et al. A single-atom library for guided monometallic and concentration-complex multimetallic designs. *Nat. Mater.* **2022**, *21*, 681–688. https://doi.org/10.1038/s41563-022-01252-y.

[10] Gerber, I. C.; Serp, P. A Theory/Experience Description of Support Effects in Carbon-Supported Catalysts. *Chem. Rev.* **2019**, *120*, 1250–1349. https://doi.org/10.1021/acs.chemrev.9b00209.

[11] Axet, M. R.; Durand, J.; Gouygou, M.; Serp, P. Surface coordination chemistry on graphene and two-dimensional carbon materials for well-defined single atom supported catalysts. In *Advances in Organometallic Chemistry*; Academic Press: Cambridge, MA, USA, 2019; pp. 53–174. https://doi.org/10.1016/bs.adomc.2019.01.002

[12] Fei, H.; Dong, J.; Chen, D.; Hu, T.; Duan, X.; Shakir, I.; Huang, Y.; Duan, X. Single atom electrocatalysts supported on graphene or graphene-like carbons. *Chem. Soc. Rev.* **2019**, *48*, 5207–5241. https://doi.org/10.1039/c9cs00422j.
[13] Navarro-Ruiz, J.; Poteau, R.; Gerber, I. C.; Del Rosal, I. Contribution of theoretical calculations to supported metal Single-Atom catalysis. In *Supported Metal Single Atom Catalysis*; Wiley Online Library: Online, 2022; pp. 241–337. https://doi.org/10.1002/9783527830169.ch7
[14] Castro Neto, A. H.; Guinea, F.; Peres, N. M. R.; Novoselov, K. S.; Geim, A. K. The electronic properties of graphene. *Rev. Mod. Phys.* **2009**, *81*, 109–162. https://doi.org/10.1103/revmodphys.81.109.
[15] Cooper, D. R.; D'anjou, B.; Ghattamaneni, N.; Harack, B.; Hilke, M.; Horth, A.; Majlis, N.; Massicotte, M.; Vandsburger, L.; Whiteway, E.; et al. Experimental Review of Graphene. *ISRN Condens. Matter Phys.* **2012**, *2012*, 1–56. https://doi.org/10.5402/2012/501686.
[16] Partoens, B.; Peeters, F. M. From graphene to graphite: Electronic structure around the **K** point. *Phys. Rev. B* **2006**, *74*, 075404. https://doi.org/10.1103/physrevb.74.075404.
[17] Rao, C. N. R.; Maitra, U.; Ramakrishna Matte, H. S. S. Synthesis, Characterization, and Selected properties of Graphene. In *Graphene: Synthesis, Properties, and Phenomena*; Rao, C. N. R., Sood, A. K., eds.; John Wiley & Sons: Hoboken, NJ, USA, 2013.
[18] Liu, L.; Ryu, S.; Tomasik, M. R.; Stolyarova, E.; Jung, N.; Hybertsen, M. S.; Steigerwald, M. L.; Brus, L. E.; Flynn, G. W. Graphene Oxidation: Thickness-Dependent Etching and Strong Chemical Doping. *Nano Lett.* **2008**, *8*, 1965–1970. https://doi.org/10.1021/nl0808684.
[19] Vittore, A.; Acocella, M. R.; Guerra, G. Edge-Oxidation of Graphites by Hydrogen Peroxide. *Langmuir* **2019**, *35*, 2244–2250. https://doi.org/10.1021/acs.langmuir.8b03489.
[20] Konradt, D.; Schroden, D.; Hagemann, U.; Heidelmann, M.; Rohns, H.-P.; Wagner, C.; Konradt, N. Kinetics of Direct Reaction of Vanadate, Chromate, and Permanganate with Graphene Nanoplatelets for Use in Water Purification. *Nanomaterials* **2024**, *14*, 140. https://doi.org/10.3390/nano14020140.
[21] Yang, Y.; Murali, R. Binding mechanisms of molecular oxygen and moisture to graphene. *Appl. Phys. Lett.* **2011**, *98*, 093116. https://doi.org/10.1063/1.3562317.
[22] *ISO/TS 80004-13:2017*; Nanotechnologies—Vocabulary—Part 13: Graphene and related Two-Dimensional (2D) Materials; International Organization for Standardization (ISO): Geneva, Switzerland, 2017.
[23] Lawrence, T.; Drzal, L. T.; Fukushima, H. Expanded Graphite and Products Produced Therefrom. US Patent US7550529B2, 23 June 2009.
[24] Kim, S.; Do, I.; Drzal, L. T. Thermal stability and dynamic mechanical behavior of exfoliated graphite nanoplatelets-LLDPE nanocomposites. *Polym. Compos.* **2009**, *31*, 755–761. https://doi.org/10.1002/pc.20781.
[25] Cataldi, P.; Athanassiou, A.; Bayer, I. S. Graphene Nanoplatelets-Based Advanced Materials and Recent Progress in Sustainable Applications. *Appl. Sci.* **2018**, *8*, 1438. https://doi.org/10.3390/app8091438.
[26] Ye, N.; Wang, Z.; Wang, S.; Fang, H.; Wang, D. Aqueous aggregation and stability of graphene nanoplatelets, graphene oxide, and reduced graphene oxide in simulated natural environmental conditions: complex roles of surface and solution chemistry. *Environ. Sci. Pollut. Res.* **2018**, *25*, 10956–10965. https://doi.org/10.1007/s11356-018-1326-6.
[27] Rasuli, H.; Rasuli, R. Nanoparticle-decorated graphene/graphene oxide: synthesis, properties and applications. *J. Mater. Sci.* **2023**, *58*, 2971–2992. https://doi.org/10.1007/s10853-023-08183-2.
[28] He, H.; Gao, C. Graphene nanosheets decorated with Pd, Pt, Au, and Ag nanoparticles: Synthesis, characterization, and catalysis applications. *Sci. China Chem.* **2011**, *54*, 397–404. https://doi.org/10.1007/s11426-010-4191-9.
[29] Mondal, A.; Jana, N. R. Surfactant-Free, Stable Noble Metal—Graphene Nanocomposite as High Performance Electrocatalyst. *ACS Catal.* **2014**, *4*, 593–599. https://doi.org/10.1021/cs401032p.
[30] Georgakilas, V.; Tiwari, J. N.; Kemp, K. C.; Perman, J. A.; Bourlinos, A. B.; Kim, K. S.; Zboril, R. Noncovalent Functionalization of Graphene and Graphene Oxide for Energy Materials, Biosensing, Catalytic, and Biomedical Applications. *Chem. Rev.* **2016**, *116*, 5464–5519. https://doi.org/10.1021/acs.chemrev.5b00620.
[31] Liu, L.; Liu, S.; Zhang, Q.; Li, C.; Bao, C.; Liu, X.; Xiao, P. Adsorption of Au (III), Pd (II), and Pt (IV) from Aqueous Solution onto Graphene Oxide. *J. Chem. Eng. Data* **2012**, *58*, 209–216. https://doi.org/10.1021/je300551c.
[32] Yin, H.; Tang, H.; Wang, D.; Gao, Y.; Tang, Z. Facile Synthesis of Surfactant-Free Au Cluster/Graphene Hybrids for High-Performance Oxygen Reduction Reaction. *ACS Nano* **2012**, *6*, 8288–8297. https://doi.org/10.1021/nn302984x.
[33] Dobrezberger, K.; Bosters, J.; Moser, N.; Yigit, N.; Nagl, A.; Föttinger, K.; Lennon, D.; Rupprechter, G. Hydrogenation on Palladium Nanoparticles Supported by Graphene Nanoplatelets. *J. Phys. Chem. C* **2020**, *124*, 23674–23682. https://doi.org/10.1021/acs.jpcc.0c06636.

[34] Daş, E.; Gürsel, S. A.; Şanlı, L. I.; Yurtcan, A. B. Thermodynamically controlled Pt deposition over graphene nanoplatelets: Effect of Pt loading on PEM fuel cell performance. *Int. J. Hydrogen Energy* **2017**, *42*, 19246–19256. https://doi.org/10.1016/j.ijhydene.2017.06.108.

[35] Ren, Y.; Rao, R.; Bhusal, S.; Varshney, V.; Kedziora, G. S.; Wheeler, R.; Kang, Y.; Roy, A.; Nepal, D. Hierarchical Assembly of Gold Nanoparticles on Graphene Nanoplatelets by Spontaneous Reduction: Implications for Smart Composites and Biosensing. *ACS Appl. Nano Mater.* **2020**, *3*, 8753–8762. https://doi.org/10.1021/acsanm.0c01555.

[36] Schmidbaur, H., Ed.; *Gold: Progress in Chemistry, Biochemistry and Technology*; John Wiley & Sons: New York, NY, USA, 1999. Lipshutz, B. H.; Yamamoto, Y. Introduction: Coinage metals in organic synthesis. *Chem. Rev.* **2008**, *108*, 2793–2795.

[37] Wiberg, E.; Wiberg, N. *Inorganic Chemistry*; Academic Press: Cambridge, MA, USA, 2001.

[38] Pettibone, J. M.; Hudgens, J. W. Gold Cluster Formation with Phosphine Ligands: Etching as a Size-Selective Synthetic Pathway for Small Clusters? *ACS Nano* **2011**, *5*, 2989–3002. https://doi.org/10.1021/nn200053b.

[39] Rocchigiani, L.; Bochmann, M. Recent Advances in Gold (III) Chemistry: Structure, Bonding, Reactivity, and Role in Homogeneous Catalysis. *Chem. Rev.* **2020**, *121*, 8364–8451. https://doi.org/10.1021/acs.chemrev.0c00552.

[40] Hashmi, A. S. K.; Hutchings, G. J. Gold Catalysis. *Angew. Chem. Int. Ed.* **2006**, *45*, 7896–7936. https://doi.org/10.1002/anie.200602454.

[41] Nkosi, B.; Coville, N.; Hutchings, G. Vapour phase hydrochlorination of acetylene with group VIII and IB metal chloride catalysts. *Appl. Catal.* **1988**, *43*, 33–39. https://doi.org/10.1016/s0166-9834(00)80898-2.

[42] Haruta, M.; Yamada, N.; Kobayashi, T.; Iijima, S. Gold catalysts prepared by coprecipitation for low-temperature oxidation of hydrogen and of carbon monoxide. *J. Catal.* **1989**, *115*, 301–309. https://doi.org/10.1016/0021-9517(89)90034-1.

[43] Renner, H.; Schlamp, G.; Kleinwächter, I.; Drost, E.; Lüschow, H. M.; Tews, P.; Panster, P.; Diehl, M.; Lang, J.; Kreuzer, T.; et al. Platinum Group Metals and Compounds. *Ullmann's Encycl. Ind. Chem.* **2001**. https://doi.org/10.1002/14356007.a21_075

[44] Mondal, A.; Jana, N. R. Effect of size and oxidation state of platinum nanoparticles on the electrocatalytic performance of graphene-nanoparticle composites. *RSC Adv.* **2015**, *5*, 85196–85201. https://doi.org/10.1039/c5ra17087g.

[45] Pfeifer, V.; Jones, T. E.; Vélez, J. J. V.; Massué, C.; Arrigo, R.; Teschner, D.; Girgsdies, F.; Scherzer, M.; Greiner, M. T.; Allan, J.; et al. The electronic structure of iridium and its oxides. *Surf. Interface Anal.* **2015**, *48*, 261–273. https://doi.org/10.1002/sia.5895.

[46] Singh, S. B. Iridium chemistry and its catalytic applications: A brief. *Green Chem. Technol. Lett.* **2016**, *2*, 206–210. https://doi.org/10.18510/gctl.2016.247.

[47] Albéniz, A. C.; Espinet, P. Palladium: Inorganic & Coordination Chemistry. *Encycl. Inorg. Chem.* **2005**. https://doi.org/10.1002/0470862106.ia178

[48] Muniz-Miranda, M.; Zoppi, A.; Muniz-Miranda, F.; Calisi, N. Palladium Oxide Nanoparticles: Preparation, Characterization and Catalytic Activity Evaluation. *Coatings* **2020**, *10*, 207. https://doi.org/10.3390/coatings10030207.

[49] Zheng, Z.; Cao, H.; Meng, J.; Xiao, Y.; Ulstrup, J.; Zhang, J.; Zhao, F.; Engelbrekt, C.; Xiao, X. Synthesis and Structure of a Two-Dimensional Palladium Oxide Network on Reduced Graphene Oxide. *Nano Lett.* **2022**, *22*, 4854–4860. https://doi.org/10.1021/acs.nanolett.2c01226.

[50] Aksoy, M.; Kilic, H.; Nişancı, B.; Metin, Ö. Recent advances in the development of palladium nanocatalysts for sustainable organic transformations. *Inorg. Chem. Front.* **2020**, *8*, 499–545. https://doi.org/10.1039/d0qi01283a.

[51] Alaqarbeh, M.; Adil, S. F.; Ghrear, T.; Khan, M.; Bouachrine, M.; Al-Warthan, A. Recent Progress in the Application of Palladium Nanoparticles: A Review. *Catalysts* **2023**, *13*, 1343. https://doi.org/10.3390/catal13101343.

[52] Abbet, S.; Sanchez, A.; Heiz, U.; Schneider, W.-D.; Ferrari, A. M.; Pacchioni, G.; Rösch, N. Acetylene Cyclotrimerization on Supported Size-Selected Pdn Clusters ($1 \leq n \leq 30$): One Atom Is Enough! *J. Am. Chem. Soc.* **2000**, *122*, 3453–3457. https://doi.org/10.1021/ja9922476.

[53] Xi, J.; Sun, H.; Wang, D.; Zhang, Z.; Duan, X.; Xiao, J.; Xiao, F.; Liu, L.; Wang, S. Confined-interface-directed synthesis of Palladium single-atom catalysts on graphene/amorphous carbon. *Appl. Catal. B Environ.* **2018**, *225*, 291–297. https://doi.org/10.1016/j.apcatb.2017.11.057.

[54] Ren, S.; Yu, Q.; Yu, X.; Rong, P.; Jiang, L.; Jiang, J. Graphene-supported metal single-atom catalysts: a concise review. *Sci. China Mater.* **2020**, *63*, 903–920. https://doi.org/10.1007/s40843-019-1286-1.

[55] Speck, F. D.; Kim, J. H.; Bae, G.; Joo, S. H.; Mayrhofer, K. J. J.; Choi, C. H.; Cherevko, S. Single-Atom Catalysts: A Perspective toward Application in Electrochemical Energy Conversion. *JACS Au* **2021**, *1*, 1086–1100. https://doi.org/10.1021/jacsau.1c00121.
[56] Dong, L.; Mazzarino, I.; Alexiadis, A. Development of Solid—Fluid Reaction Models—A Literature Review. *Chemengineering* **2021**, *5*, 36. https://doi.org/10.3390/chemengineering5030036.
[57] Choi, B.; Lee, J.; Lee, S.; Ko, J.; Lee, K.; Oh, J.; Han, J.; Kim, Y.; Choi, I. S.; Park, S. Generation of Ultra-High-Molecular-Weight Polyethylene from Metallocenes Immobilized onto N-Doped Graphene Nanoplatelets. *Macromol. Rapid Commun.* **2013**, *34*, 533–538. https://doi.org/10.1002/marc.201200768.
[58] Li, X.; Mitchell, S.; Fang, Y.; Li, J.; Perez-Ramirez, J.; Lu, J. Advances in heterogeneous single-cluster catalysis. *Nat. Rev. Chem.* **2023**, *7*, 754–767. https://doi.org/10.1038/s41570-023-00540-8.
[59] Jeong, H.; Shin, D.; Kim, B.; Bae, J.; Shin, S.; Choe, C.; Han, J. W.; Lee, H. Controlling the Oxidation State of Pt Single Atoms for Maximizing Catalytic Activity. *Angew. Chem. Int. Ed.* **2020**, *59*, 20691–20696. https://doi.org/10.1002/anie.202009776.
[60] Zhu, Y.; Ji, H.; Cheng, H.-M.; Ruoff, R. S. Mass production and industrial applications of graphene materials. *Natl. Sci. Rev.* **2018**, *5*, 90–101. https://doi.org/10.1093/nsr/nwx055.
[61] Xia, Y.; Tian, H.; Li, Y.; Yang, X.; Liu, J.; Liu, C.; Zhou, L.; Zhang, L.; Li, T.; Shi, T. Kinetic Analysis of the Reduction Processes of a Cisplatin Pt (IV) Prodrug by Mesna, Thioglycolic Acid, and Thiolactic Acid. *J. Chem.* **2020**, *2020*, 1–12. https://doi.org/10.1155/2020/5868174.
[62] Peck, J. A.; Tait, C.; Swanson, B. I.; Brown, G. E. Speciation of aqueous gold (III) chlorides from ultraviolet/visible absorption and Raman/resonance Raman spectroscopies. *Geochim. et Cosmochim. Acta* **1991**, *55*, 671–676. https://doi.org/10.1016/0016-7037(91)90332-y.
[63] Peters, D. G.; Lingane, J. J. Anodic formation and chemical analysis of oxychloride films on platinum electrodes. *J. Electroanal. Chem. (1959)* **1962**, *4*, 193–217. https://doi.org/10.1016/0022-0728(62)80048-5.
[64] Weusten, S.; de Groot, M.; van der Schaaf, J. A comparative study of the stability of hexachloroiridate and hexacyanoferrate in electrochemical mass transfer measurements. *J. Electroanal. Chem.* **2020**, *878*, 114512. https://doi.org/10.1016/j.jelechem.2020.114512.
[65] Rasmussen, L.; Jørgensen, C. K.; Sjövall, J.; Zaidi, N. A. Palladium (II) Complexes. I. Spectra and Formation Constants of Ammonia and Ethylenediamine Complexes. *Acta Chem. Scand.* **1968**, *22*, 2313–2323. https://doi.org/10.3891/acta.chem.scand.22-2313.
[66] Elding, L. I.; Olsson, L. F. Electronic absorption spectra of square-planar chloro-aqua and bromo-aqua complexes of palladium (II) and platinum (II). *J. Phys. Chem.* **1978**, *82*, 69–74. https://doi.org/10.1021/j100490a018.
[67] Tran, H. N. Differences between Chemical Reaction Kinetics and Adsorption Kinetics: Fundamentals and Discussion. *J. Tech. Educ. Sci.* **2022**, 33–47. https://doi.org/10.54644/jte.70b.2022.1154.
[68] Robati, D. Pseudo-second-order kinetic equations for modeling adsorption systems for removal of lead ions using multi-walled carbon nanotube. *J. Nanostructure Chem.* **2013**, *3*, 55. https://doi.org/10.1186/2193-8865-3-55.
[69] Revellame, E. D.; Fortela, D. L.; Sharp, W.; Hernandez, R.; Zappi, M. E. Adsorption kinetic modeling using pseudo-first order and pseudo-second order rate laws: A review. *Clean. Eng. Technol.* **2020**, *1*, 100032. https://doi.org/10.1016/j.clet.2020.100032.
[70] Bevington, P. R.; Robinson, D. K. *Data Reduction and Error Analysis for the Physical Sciences*, 3rd ed.; Mc. Graw Hill: Boston, MA, USA, 2003; pp. 98–115.
[71] Jørgensen, C. K.; Bresle, Å.; Ormerod, J. G.; Stenhagen, E.; Thorell, B. Complexes of the 4d- and 5d-Groups. II. Crystal Field and Electron Transfer Spectra of Ruthenium (II) and (III), Iridium (IV), and Platinum (IV). *Acta Chem. Scand.* **1956**, *10*, 518–534. https://doi.org/10.3891/acta.chem.scand.10-0518.
[72] Lingane, J. J. Standard potentials of half-reactions involving +1 and +3 gold in chloride medium. *J. Electroanal. Chem. (1959)* **1962**, *4*, 332–342. https://doi.org/10.1016/0022-0728(62)80079-5.
[73] Latimer, W. M. *Oxidation Potentials*; Prentice-Hall, Inc.: New York, NY, USA, 1952.
[74] Jackson, E.; Pantony, D. A. Investigations in platinum metal group electrochemistry: I some iridium (IV) ? iridium (III) systems. *J. Appl. Electrochem.* **1971**, *1*, 113–126. https://doi.org/10.1007/bf01111858.
[75] Jackson, E.; Pantony, D. A. Investigations in platinum metal group electrochemistry: II The Pd(II)-Pd° reduction. *J. Appl. Electrochem.* **1971**, *1*, 283–291. https://doi.org/10.1007/bf00688651.
[76] Fraga, T. J. M.; Sobrinho, M. A.d.M.; Carvalho, M. N.; Ghislandi, M. G. State of the art: synthesis and characterization of functionalized graphene nanomaterials. *Nano Express* **2020**, *1*, 022002. https://doi.org/10.1088/2632-959X/abb921.

[77] Garratt-Reed, A. J.; Bell, D. C.; Patrick, N. *Energy-Dispersive X-ray Analysis in the Electron Microscope*; Bios Scientific Publishers, Ltd.: Oxford, UK, 2003; p. 126, ISBN 1859961096.

[78] von Harrach, H.; Klenov, D.; Freitag, B.; Schlossmacher, P.; Collins, P.; Fraser, H. Comparison of the Detection Limits of EDS and EELS in S/TEM. *Microsc. Microanal.* **2010**, *16*, 1312–1313. https://doi.org/10.1017/s1431927610058940.

[79] Kong, B.-S.; Geng, J.; Jung, H.-T. Layer-by-layer assembly of graphene and gold nanoparticles by vacuum filtration and spontaneous reduction of gold ions. *Chem. Commun.* **2009**, 2174–2176. https://doi.org/10.1039/b821920f.

[80] Huang, H.; Zhou, J.; Xie, M.; Liu, H. Mechanistic Study on Graphene Oxidation by $KMnO_4$ in Solution Phase and Resultant Carbon-Carbon Unzipping. *J. Phys. Chem. C* **2020**, *124*, 11165–11173. https://doi.org/10.1021/acs.jpcc.0c01314.

[81] Freakley, S. J.; Ruiz-Esquius, J.; Morgan, D. J. The X-ray photoelectron spectra of Ir, IrO_2 and $IrCl_3$ revisited. *Surf. Interface Anal.* **2017**, *49*, 794–799. https://doi.org/10.1002/sia.6225.

[82] Jeong, B.; Lee, D.; Park, J.-I.; Lee, S. M. Near ambient pressure XPS investigation of hydrous palladium oxide under water and oxygen gas environments. *J. Phys. D Appl. Phys.* **2021**, *54*, 324001. https://doi.org/10.1088/1361-6463/ac0183.

[83] Available online: https://www.xpsfitting.com/search/label/Palladium (accessed on 28 April 2024).

[84] Scheerder, J. E.; Liu, S.; Zharinov, V. S.; Reckinger, N.; Colomer, J.; Cheng, H.; Van de Vondel, J.; Janssens, E. Electronic Detection of Oxygen Adsorption and Size-Specific Doping of Few-Atom Gold Clusters on Graphene. *Adv. Mater. Interfaces* **2018**, *5*. https://doi.org/10.1002/admi.201801274.

[85] Wojnicki, M.; Luty-Błocho, M.; Socha, R. P.; Mech, K.; Pędzich, Z.; Fitzner, K.; Rudnik, E. Kinetic studies of sorption and reduction of gold (III) chloride complex ions on activated carbon Norit ROX 0.8. *J. Ind. Eng. Chem.* **2015**, *29*, 289–297. https://doi.org/10.1016/j.jiec.2015.03.036.

[86] Wojnicki, M.; Luty-Błocho, M.; Socha, R. P.; Pędzich, Z.; Małecki, S.; Kula, A.; Żabiński, P. The kinetic studies of gold (III) chloride complex adsorption mechanism from an aqueous and semi-aqueous system. *J. Mol. Liq.* **2019**, *278*, 43–52. https://doi.org/10.1016/j.molliq.2019.01.028.

[87] Shi, Y.; Kim, K. K.; Reina, A.; Hofmann, M.; Li, L.-J.; Kong, J. Work Function Engineering of Graphene Electrodevia Chemical Doping. *ACS Nano* **2010**, *4*, 2689–2694. https://doi.org/10.1021/nn1005478.

[88] Kim, B.-J.; Yang, G.; Kim, H.-Y.; Baik, K. H.; Mastro, M. A.; Hite, J. K.; Eddy, C. R.; Ren, F.; Pearton, S. J.; Kim, J. GaN-based ultraviolet light-emitting diodes with $AuCl_3$-doped graphene electrodes. *Opt. Express* **2013**, *21*, 29025–29030. https://doi.org/10.1364/oe.21.029025.

[89] Scheerder, J. E.; Picot, T.; Reckinger, N.; Sneyder, T.; Zharinov, V. S.; Colomer, J.-F.; Janssens, E.; Van de Vondel, J. Decorating graphene with size-selected few-atom clusters: a novel approach to investigate graphene—adparticle interactions. *Nanoscale* **2017**, *9*, 10494–10501. https://doi.org/10.1039/C7NR02217D.

[90] Amft, M.; Sanyal, B.; Eriksson, O.; Skorodumova, N. V. Small gold clusters on graphene, their mobility and clustering: a DFT study. *J. Phys. Condens. Matter* **2011**, *23*, 205301–205301. https://doi.org/10.1088/0953-8984/23/20/205301.

[91] Manadé, M.; Viñes, F.; Illas, F. Transition metal adatoms on graphene: A systematic density functional study. *Carbon* **2015**, *95*, 525–534. https://doi.org/10.1016/j.carbon.2015.08.072.

[92] McCreary, K. M.; Pi, K.; Swartz, A. G.; Han, W.; Bao, W.; Lau, C. N.; Guinea, F.; Katsnelson, M. I.; Kawakami, R. K. Effect of cluster formation on graphene mobility. *Phys. Rev. B* **2010**, *81*, 115453. https://doi.org/10.1103/physrevb.81.115453.

[93] Hardcastle, T. P.; Seabourne, C. R.; Zan, R.; Brydson, R. M. D.; Bangert, U.; Ramasse, Q. M.; Novoselov, K. S.; Scott, A. J. Mobile metal adatoms on single layer, bilayer, and trilayer graphene: Anab initioDFT study with van der Waals corrections correlated with electron microscopy data. *Phys. Rev. B* **2013**, *87*, 195430. https://doi.org/10.1103/physrevb.87.195430.

[94] Wang, H.; Li, K.; Cheng, Y.; Wang, Q.; Yao, Y.; Schwingenschlögl, U.; Zhang, X.; Yang, W. Interaction between single gold atom and the graphene edge: A study via aberration-corrected transmission electron microscopy. *Nanoscale* **2012**, *4*, 2920–2925. https://doi.org/10.1039/c2nr00059h.

[95] Pavlovic, Z.; Ranjan, C.; Gao, Q.; van Gastel, M.; Schlögl, R. Probing the Structure of a Water-Oxidizing Anodic Iridium Oxide Catalyst using Raman Spectroscopy. *ACS Catal.* **2016**, *6*, 8098–8105. https://doi.org/10.1021/acscatal.6b02343.

[96] Ali, I.; AlGhamdi, K.; Al-Wadaani, F. T. Advances in iridium nano catalyst preparation, characterization and applications. *J. Mol. Liq.* **2019**, *280*, 274–284. https://doi.org/10.1016/j.molliq.2019.02.050.

[97] Wojnicki, M.; Socha, R. P.; Luty-Błocho, M.; Fitzner, K. Kinetic studies of the removal of Pt (IV) chloride complex ions from acidic aqueous solutions using activated carbon. *React. Kinet. Catal. Lett.* **2017**, *120*, 715–734. https://doi.org/10.1007/s11144-017-1151-9.

[98] Fampiou, I.; Ramasubramaniam, A. Binding of Pt Nanoclusters to Point Defects in Graphene: Adsorption, Morphology, and Electronic Structure. *J. Phys. Chem. C* **2012**, *116*, 6543–6555. https://doi.org/10.1021/jp2110117.

[99] Bord, J.; Kirchhoff, B.; Baldofski, M.; Jung, C.; Jacob, T. An Atomistic View of Platinum Cluster Growth on Pristine and Defective Graphene Supports. *Small* **2023**, *19*, e2207484. https://doi.org/10.1002/smll.202207484.

[100] Okazaki-Maeda, K.; Morikawa, Y.; Tanaka, S.; Kohyama, M. Structures of Pt clusters on graphene by first-principles calculations. *Surf. Sci.* **2009**, *604*, 144–154. https://doi.org/10.1016/j.susc.2009.11.001.

[101] Qi, Q.; Liu, H.; Feng, W.; Tian, H.; Xu, H.; Huang, X. Theoretical investigation on the interaction of subnano platinum clusters with graphene using DFT methods. *Comput. Mater. Sci.* **2015**, *96*, 268–276. https://doi.org/10.1016/j.commatsci.2014.09.033.

[102] Yan, H.; Lin, Y.; Wu, H.; Zhang, W.; Sun, Z.; Cheng, H.; Liu, W.; Wang, C.; Li, J.; Huang, X.; et al. Bottom-up precise synthesis of stable platinum dimers on graphene. *Nat. Commun.* **2017**, *8*, 1–11. https://doi.org/10.1038/s41467-017-01259-z.

[103] Wojnicki, M.; Socha, R. P.; Pędzich, Z.; Mech, K.; Tokarski, T.; Fitzner, K. Palladium (II) Chloride Complex Ion Recovery from Aqueous Solutions Using Adsorption on Activated Carbon. *J. Chem. Eng. Data* **2018**, *63*, 702–711. https://doi.org/10.1021/acs.jced.7b00885.

[104] Wojnicki, M.; Fitzner, K. Kinetic modeling of the adsorption process of Pd (II) complex ions onto activated carbon. *React. Kinet. Catal. Lett.* **2018**, *124*, 453–468. https://doi.org/10.1007/s11144-018-1412-2.

[105] Ramos-Castillo, C.; Reveles, J.; Zope, R.; de Coss, R. Palladium Clusters Supported on Graphene Monovacancies for Hydrogen Storage. *J. Phys. Chem. C* **2015**, *119*, 8402–8409. https://doi.org/10.1021/acs.jpcc.5b02358.

[106] Cabria, I.; López, M. J.; Alonso, J. A. Theoretical study of the transition from planar to three-dimensional structures of palladium clusters supported on graphene. *Phys. Rev. B* **2010**, *81*. https://doi.org/10.1103/physrevb.81.035403.

[107] Kaur, G.; Gupta, S.; Dharamvir, K. Palladium dimers adsorbed on graphene: A DFT study. In Proceedings of the International Conference on Condensed Matter Physics 2014 (ICCMP 2014), Shimla, India, 4–6 November 2014.

[108] Uhlig, M. R.; Martin-Jimenez, D.; Garcia, R. Atomic-scale mapping of hydrophobic layers on graphene and few-layer MoS2 and WSe2 in water. *Nat. Commun.* **2019**, *10*, 1–7. https://doi.org/10.1038/s41467-019-10740-w.

[109] Dong, L.; Mazzarino, I.; Alexiadis, A. Development of Solid—Fluid Reaction Models—A Literature Review. *Chemengineering* **2021**, *5*, 36. https://doi.org/10.3390/chemengineering5030036.

[110] Xi, J.; Jung, H. S.; Xu, Y.; Xiao, F.; Bae, J. W.; Wang, S. Synthesis Strategies, Catalytic Applications, and Performance Regulation of Single-Atom Catalysts. *Adv. Funct. Mater.* **2021**, *31*. https://doi.org/10.1002/adfm.202008318.

[111] Li, S.; Kan, Z.; Wang, H.; Bai, J.; Liu, Y.; Liu, S.; Wu, Y. Single-atom photo-catalysts: Synthesis, characterization, and applications. *Nano Mater. Sci.* **2023**. https://doi.org/10.1016/j.nanoms.2023.11.001.